

SIMPLE MODELS OF METAL-LINE ABSORPTION AND EMISSION FROM COOL GAS OUTFLOWS

J. XAVIER PROCHASKA¹, DANIEL KASEN^{2,3}, KATE RUBIN¹*Draft version October 25, 2018*

ABSTRACT

We analyze the absorption and emission-line profiles produced by a set of simple, cool gas wind models motivated by galactic-scale outflow observations. We implement monte carlo radiative transfer techniques that track the propagation of scattered and fluorescent photons to generate 1D spectra and 2D spectral images. We focus on the Mg II $\lambda\lambda 2796, 2803$ doublet and Fe II UV1 multiplet at $\lambda \approx 2600\text{\AA}$, but the results are applicable to other transitions that trace outflows (e.g. Na I, H I Ly α , Si II). By design, the resonance transitions show blue-shifted absorption but one also predicts strong resonance and fine-structure line-emission at roughly the systemic velocity. This line-emission ‘fills-in’ the absorption reducing the equivalent width by up to 50%, shift the absorption-line centroid by tens of km s^{-1} , and reduce the effective opacity near systemic. Analysis of cool gas outflows that ignores this line-emission may incorrectly infer that the gas is partially covered, measure a significantly lower peak optical depth, and/or conclude that gas at systemic velocity is absent (e.g. an interstellar or slowly infalling component). Because the Fe II lines are connected by optically-thin transitions to fine-structure levels, their profiles more closely reproduce the intrinsic opacity of the wind. Together these results naturally explain the absorption and emission-line characteristics observed for star-forming galaxies at $z < 1$. We also study a scenario promoted to describe the outflows of $z \sim 3$ Lyman break galaxies and find profiles inconsistent with the observations due to scattered photon emission. Although line-emission complicates the analysis of absorption-line profiles, the surface brightness profiles offer a unique means of assessing the morphology and size of galactic-scale winds. Furthermore, the kinematics and line-ratios offer powerful diagnostics of outflows, motivating deep, spatially-extended spectroscopic observations.

Subject headings: galaxies: formation – galaxies: starburst

1. INTRODUCTION

Nearly all gaseous objects that shine are also observed to generate gaseous flows. This includes the jets of protostars, the stellar winds of massive O and B stars, the gentle Solar wind of our Sun, the associated absorption of bright quasars, and the spectacular jets of radio-loud AGN. These gaseous outflows regulate the metal and dust content and distribution within the objects and their surroundings, moderate the accretion of new material, and inject energy and momentum into gas on large scales. Developing a comprehensive model for these flows is critical to understanding the evolution of the source and its impact on the surrounding environment.

Starburst galaxies, whose luminosity is dominated by H II regions and massive stars, are also observed to drive gaseous outflows. These flows are generally expected (and sometimes observed) to have multiple phases, for example a hot and diffuse phase traced by X-ray emission together with a cool, denser phase traced by H α emission (e.g. Heckman et al. 1990; Martin 1999; Strickland et al. 2004; Kobulnicky & Martin 2010). Several spectacular examples in the local universe demonstrate that flows can extend to up to ~ 10 kpc from the galaxy (Lehnert et al. 1999; Veilleux et al. 2003; Westmoquette et al. 2008)

carrying significant speed to escape from the gravitational potential well of the galaxy’s dark matter halo (e.g. Strickland & Heckman 2009).

Galactic outflows are also revealed by UV and optical absorption lines, e.g. Na I, Mg II, Si II and C IV transitions. With the galaxy as a backlight, one observes gas that is predominantly blue-shifted which indicates a flow toward Earth and away from the galaxy. These transitions are sensitive to the cool (Mg II; $T \sim 10^4\text{K}$) and warm (C IV; $T \sim 10^5\text{K}$) phases of the flow. The incidence of cool gas outflows is nearly universal in vigorously star-forming galaxies; this includes systems at low z which exhibit Na I and Mg II absorption (Rupke et al. 2005a; Martin 2005; Sato et al. 2009; Martin & Bouché 2009; Chen et al. 2010), $z \sim 1$ star-forming galaxies with winds traced by Fe II and Mg II transitions (Weiner et al. 2009; Rubin et al. 2010b), and $z > 2$ Lyman break galaxies (LBGs) that show blue-shifted Si II, C II, and O I transitions (Steidel et al. 1996; Lowenthal et al. 1997; Shapley et al. 2003).

The observation of metal-line absorption is now a well-established means of identifying outflows. Furthermore, because the X-ray and H α emission generated by winds is faint, absorption-line analyses have traditionally been the only way to probe outflows in distant galaxies. However, very little research has been directed toward comparing the observations against (even idealized) wind models (e.g. Fujita et al. 2009). Instead, researchers have gleaned what limited information is afforded by direct analysis of the absorption lines. The data diagnose the speed of the gas relative to the galaxy, yet

¹ Department of Astronomy and Astrophysics, UCO/Lick Observatory, University of California, 1156 High Street, Santa Cruz, CA 95064

² Departments of Physics and Astronomy, University of California, Berkeley, 366 LeConte Hall, Berkeley CA, 94720

³ Nuclear Science Division, Lawrence Berkeley National Laboratory, 1 Cyclotron Rd, Berkeley, CA, 94720

they poorly constrain the optical depth, covering fraction, density, temperature, and distance of the flow from the galaxy. In turn, constraints related to the mass, energetics, and momentum of the flow suffer from orders of magnitude uncertainty. Both the origin and impact of galactic-scale winds, therefore, remain open matters of debate (Murray et al. 2005; Socrates et al. 2008; Strickland & Heckman 2009; Simcoe et al. 2002; Oppenheimer & Davé 2006; Kereš et al. 2009).

Recent studies of $z \lesssim 1$ star-forming galaxies have revealed that the cool outflowing gas often exhibits significant resonant-line emission (e.g. Mg II, Na I) in tandem with the nearly ubiquitous blue-shifted absorption (Weiner et al. 2009; Martin & Bouché 2009; Rubin et al. 2010b; Chen et al. 2010). The resultant spectra resemble the P-Cygni profile characteristic of stellar winds. This phenomenon was first reported by Phillips (1993), who observed blue-shifted absorption and red-shifted emission for the Na I transition in the spectrum of the local starburst galaxy NGC 1808. More recently, Weiner et al. (2009), who studied Mg II absorption in $z \sim 1.4$ galaxies, reported Mg II emission in a small subset of the individual galaxy spectra of their large sample. These were excluded from the full analysis on concerns that the emission was related to AGN activity. The stacked spectra of the remaining galaxies, however, also indicated Mg II emission, both directly and when the authors modeled and ‘removed’ the $v \approx 0 \text{ km s}^{-1}$ absorption component. The authors suggested the emission could be related to back-scattered light in the wind, but presumed that it was related to weak AGN activity. Very similar Mg II emission was observed by Rubin et al. (2010b) who repeated the analysis of Weiner et al. (2009) on a set of lower redshift galaxies.

Bright Mg II line emission has also been reported for individual galaxies at $z \sim 0.7$ by (Rubin et al. 2010a, see also Rubin et al. 2011, in prep.). In their analysis of a single galaxy spectrum, Rubin et al. (2010a) further demonstrated that the Mg II line emission is spatially extended, and used the size of the emission to infer that the wind extends to at least 7 kpc from the galaxy. These authors additionally detected line emission from non-resonant Fe II* transitions, and attributed the emission to fluorescence powered by Fe II resonant absorption. In other words, these photons are re-emitted by the wind into our sightline, and are analogous to the emitted photons in a P-Cygni profile. Line-emission that may be related to outflows is also observed for $z \sim 3$ LBGs in the resonant Ly α transition and non-resonant Si II* transitions⁴ (Pettini et al. 2002; Shapley et al. 2003). This emission likely arises from a completely different physical process than those generating X-ray and H α emission (e.g., shocks), and presumably probes both the cool gas at the base of the wind and the outskirts of the flow (i.e., wherever a given transition is optically thick). A comprehensive analysis of the scattered and fluorescent emission related to galactic-scale outflows (e.g. via deep integral-field-unit [IFU] observations, Swinbank et al. 2005; Westmoquette et al. 2008) may offer unique diagnostics on the spatial extent, morphology, and density of the outflow from distant galaxies, eventually setting tighter constraints on the energetics of

TABLE 1
Mg II AND Fe II TRANSITIONS CONSIDERED

	E_{high} (cm^{-1})	E_{low} (cm^{-1})	J_{high}	J_{low}	λ (\AA)	A (s^{-1})
Fe II UV1	38458.98	0.00	9/2	9/2	2600.173	2.36E+08
	38458.98	384.79	9/2	7/2	2626.451	3.41E+07
	38660.04	0.00	7/2	9/2	2586.650	8.61E+07
	38660.04	384.79	7/2	7/2	2612.654	1.23E+08
	38660.04	667.68	7/2	5/2	2632.108	6.21E+07
	38858.96	667.68	5/2	5/2	2618.399	4.91E+07
	38858.96	862.62	5/2	3/2	2631.832	8.39E+07
Mg II	35760.89	0.00	3/2	0	2796.351	2.63E+08
	35669.34	0.00	1/2	0	2803.528	2.60E+08

NOTE. — Atomic data from Morton (2003).

the flow.

Although astronomers are rapidly producing a wealth of observational datasets on galactic-scale winds, a key ingredient to a proper analysis is absent. Just as comparisons between observed supernova lightcurves and spectra and radiative transfer calculations of SNe models have provided crucial insight into the physics driving, e.g., standard candle relationships for both Type Ia and IIP SNe (Kasen & Woosley 2007, 2009), modeling of the observable signatures of galactic outflows is necessary for understanding the physical properties of the gas and ultimately the physics driving the flows. In this paper, we take the first steps toward modeling the absorption and emission properties of cool gas outflows as observed in one dimensional spectra and by IFUs. Using Monte Carlo radiative transfer techniques, we study the nature of Mg II and Fe II absorption and emission for winds with a range of properties, accounting for the effects of resonant scattering and fluorescence. Although the winds are idealized, the results frequently contradict our intuition and challenge the straightforward conversion of observables to (even crude) physical constraints. These findings have a direct bearing on recent and upcoming surveys of galactic outflows, particularly those which make use of Mg II and Fe II transitions to probe outflow properties.

The paper is organized as follows. In § 2, we describe the methodology of our radiative transfer algorithms. These are applied to a fiducial wind model in § 3 and variations of this model in § 4. In § 5, we explore wind models with a broader range of density and velocity laws. We discuss the principal results and connect to observations in § 6. A brief summary is given in § 7.

2. METHODOLOGY

This section describes our methodology for generating emission/absorption profiles from simple wind models.

2.1. The Radiative Transitions

In this paper, we focus on two sets of radiative transitions arising from Fe⁺ and Mg⁺ ions (Table 1, Figure 1). This is a necessarily limited set, but the two ions and their transitions do have characteristics shared by the majority of low-ion transitions observed in cool-gas outflows. Therefore, many of the results that follow may be generalized to observational studies that consider other atoms and ions tracing cool gas.

The Mg⁺ ion, with a single 3s electron in the ground-state, exhibits an alkali doublet of transitions at $\lambda \approx$

⁴ See also France et al. (2010) for a new example at $z \sim 0$.

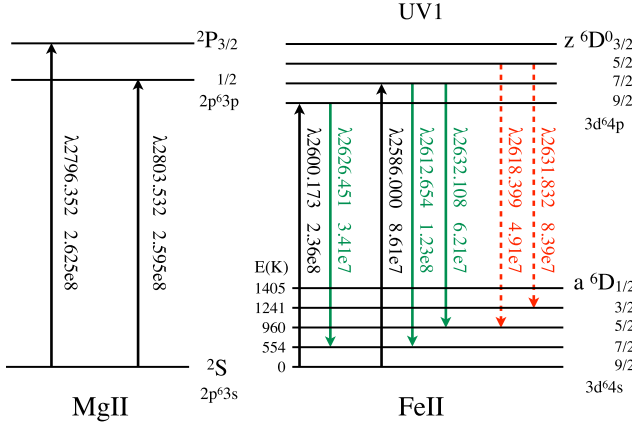


FIG. 1.— Energy level diagrams for the Mg II $\lambda\lambda 2796, 2803$ doublet and the UV1 multiplet of Fe II transitions (based on Figure 7 from Hartigan et al. (1999)). Each transition shown is labeled by its rest wavelength (Å) and Einstein A-coefficient (s^{-1}). Black upward arrows indicate the resonance-line transitions, i.e. those connected to the ground state. The $2p^63p$ configuration of Mg^+ is split into two energy levels that give rise to the Mg II $\lambda\lambda 2796, 2803$ doublet. Both the $3d^64s$ ground state and $3d^64p$ upper level of Fe^+ exhibit fine-structure splitting that gives rise to a series of electric-dipole transitions. The downward (green) arrows show the Fe II* transitions that are connected to the resonance-line transitions (i.e. they share the same upper energy levels). We also show a pair of transitions (Fe II* $\lambda\lambda 2618, 2631$; red and dashed lines) that arise from higher levels in the $z\ 6D^0$ configuration. These transitions have not yet been observed in galactic-scale outflows and are not considered in our analysis.

2800Å analogous to the Ly α doublet of neutral hydrogen. Figure 1 presents the energy level diagram for this Mg II $\lambda\lambda 2796, 2803$ doublet. In non-relativistic quantum mechanics, the $2p^63p$ energy level is said to be split by spin-orbit coupling giving the observed line doublet. These are the only Mg II electric-dipole transitions with wavelengths near 2800Å and the transition connecting the $2P_{3/2}$ and $2P_{1/2}$ states is forbidden by several selection rules. Therefore, an absorption from $2p^63s \rightarrow 2p^63p$ is followed $\approx 100\%$ of the time by a spontaneous decay ($t_{\text{decay}} \approx 4 \times 10^{-9}s$) to the ground state. Our treatment will ignore any other possibilities (e.g. absorption by a second photon when the electron is at the $2p^63p$ level).

In terms of radiative transfer, the Mg II $\lambda\lambda 2796, 2803$ doublet is very similar to that for H I Ly α , the Na I $\lambda\lambda 5891, 5897$ doublet, and many other doublets commonly studied in the interstellar medium (ISM) of distant galaxies. Each of these has the ground-state connected to a pair of electric dipole transitions with nearly identical energy. The doublets differ only in their rest wavelengths and the energy of the doublet separation. For H I Ly α , the separation is sufficiently small ($\Delta v = c\Delta E/E \approx 1.3 \text{ km s}^{-1}$) that most radiative transfer treatments actually ignore it is a doublet. This is generally justifiable for Ly α because most astrophysical processes have turbulent motions that significantly exceed the doublet’s velocity separation and effectively mix the two transitions. For Mg II ($\Delta v \approx 770 \text{ km s}^{-1}$), Na I ($\Delta v \approx 304 \text{ km s}^{-1}$), and most of the other doublets commonly observed, the separation is large and the transitions must be treated separately.

Iron exhibits the most complex set of energy levels for elements frequently studied in astrophysics. The Fe^+ ion alone has millions of energy levels recorded (Kurucz 2005), and even this is an incomplete list. One reason for iron’s complexity is that the majority of its configurations exhibit fine-structure splitting. This includes the ground-state configuration ($a\ 6D^0$) which is split into 5 levels, labeled by the total angular momentum J , with excitation energies $T_{\text{ex}} \equiv \Delta E/k$ ranging from $T_{\text{ex}} \approx 500 - 1500 \text{ K}$ (Figure 1). Transitions between these fine-structure levels are forbidden (magnetic-dipole) and have spontaneous decay times of several hours.

In this paper, we examine transitions between the ground-state configuration and the energy levels of the $z\ 6D^0$ configuration. This set of transitions (named the UV1 multiplet) have wavelengths near 2600Å. There are two resonance-line transitions⁵ associated with this multiplet (Fe II $\lambda\lambda 2586, 2600$) corresponding to $\Delta J = 0, -1$; these are indicated by upward (black) arrows in Figure 1. The solid (green) downward arrows in Figure 1 mark the non-resonant Fe II* transitions that are connected to the upper energy levels of the resonance lines. These transitions may occur following the absorption of a single photon by Fe^+ in its ground-state. This process may also be referred to as fluorescence. Note that two of these transitions (Fe II* $\lambda\lambda 2626, 2632$) are close enough in energy that their line profiles can overlap.

The Figure also shows (as dashed, downward arrows) two of the Fe II* transitions that connect to higher energy levels of the $z\ 6D^0$ configuration. Ignoring collisions and recombinations, these transitions may only occur after the absorption of two photons: one to raise the electron from the ground-state to an excited state and another to raise the electron from the excited state to one of the $z\ 6D^0$ levels with $J \leq 5/2$. The excitation of fine-structure levels by the absorption of UV photons is termed indirect UV pumping (e.g Silva & Viegas 2002; Prochaska et al. 2006) and requires the ion to lie near an intense source of UV photons. Even a bright, star-forming galaxy emits too few photons at $\lambda \approx 2500\text{Å}$ to UV-pump Fe^+ ions that are farther than $\sim 100 \text{ pc}$ from the stars. In the following, we will assume that emission from this process is negligible.

Our calculations also ignore collisional processes⁶, i.e. collisional excitation and de-excitation of the various levels. For the fine-structure levels of the $a\ 6D^0$ configuration, the excitation energies are modest ($T_{\text{ex}} \sim 1000 \text{ K}$) but the critical density n_c is large. For the $a\ 6D^0_{9/2} \rightarrow a\ 6D^0_{7/2}$ transition, the critical density $n_c^C \approx 4 \times 10^5 \text{ cm}^{-3}$. At these densities, one would predict detectable quantities of Fe I which has not yet been observed in galactic-scale outflows. If collisional excitation is insignificant then one may also neglect collisional de-excitation. Furthermore, observations rarely show *absorption* from the fine-structure levels of the $a\ 6D^0$ configuration and that material is not significantly blue-shifted (Rubin et al., in prep). In the following, we assume that electrons only occupy the ground-state, i.e. the gas has zero opacity to the non-resonant lines. Regarding the

⁵ We adopt the standard convention that a “resonance line” is an electric-dipole transition connected to the ground-state. We also label non-resonant transitions with an asterisk, e.g. Fe II* $\lambda 2612$.

⁶ Recombination is also ignored.

Mg II doublet, its excitation energy is significantly higher implying negligible collisional processes at essentially any density.

2.2. The Source

Nearly all of the absorption studies of galactic-scale outflows have focused on intensely, star-forming galaxies. The intrinsic emission of these galaxies is a complex combination of light from stars and H II regions that is then modulated by dust and gas within the ISM. For the spectral regions studied here, the hottest stars show a featureless continuum, but later spectral types do show significant Mg II and Fe II absorption. In addition, asymmetric and/or blue-shifted absorption is exhibited in these transitions in A and F stars driving stellar winds (Snow et al. 1994). Mg II P Cygni profiles are observed in a handful of F stars by Snow et al. (1994), who attribute the emission to chromospheric activity rather than mass-loss effects. H II regions, meanwhile, are observed to emit weakly at the Mg II $\lambda\lambda 2796, 2803$ doublet, primarily due to recombinations in the outer layers (Kinney et al. 1993). It is beyond the scope of this paper to properly model the stellar absorption and H II region emission, but the reader should be aware that they can complicate the observed spectrum, independently of any outflow, especially at velocities $v \approx 0 \text{ km s}^{-1}$. In the following, we assume a simple flat continuum normalized to unit value. The size of the emitting region r_{source} is a free parameter, but we restrict its value to be smaller than the minimum radial extent of any gaseous component. Lastly, the source does not absorb any scattered or emitted photons.

2.3. Monte Carlo Algorithm

We calculated spectra using a 3D Monte Carlo radiation transport code originally designed for supernova outflows (Kasen et al. 2006) but modified to treat resonant line transport on a galactic scale (Kasen et al. 2010). Our methods are similar to those used in several other codes which focus on Ly α (e.g., Zheng & Miralda-Escudé 2002; Dijkstra et al. 2006; Verhamme et al. 2006; Laursen et al. 2009), except that here we include the effects of multiple line scattering and fluorescence.

For our 3-dimensional calculations, the wind properties (density, temperature and velocity) were discretized on a 300^3 Cartesian grid (for certain 1-D calculations, the wind properties were simply computed on the fly from analytic formulae). The radiation field was represented by N photon packets (typically $N \sim 10^7$) which were initially emitted isotropically and uniformly throughout the source region ($r < r_{\text{source}}$). The wavelengths of the packets were sampled from a flat spectral energy distribution.

Photon packets were tracked through randomized scattering and absorption events until they escaped the computational domain. The distance to the next packet interaction event was determined by Doppler shifting packets to the comoving frame and sampling the mean free path to each resonance line (and dust, if present). The resonant line opacity followed a Voigt profile which was determined using the analytic fits of Tasitsiomi (2006). Non-resonant lines were assumed to be completely opti-

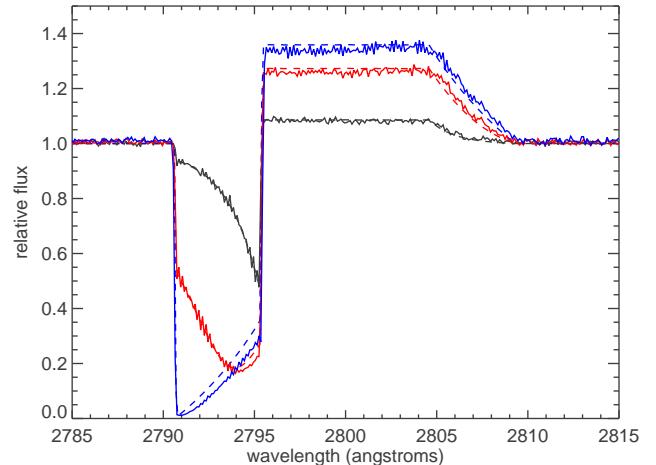


FIG. 2.— Line profiles of a test problem calculated using the monte carlo code (solid) and by direct numerical integration of the transport equation under the Sobolev approximation (dashed lines). The configuration was spherical and consisted of a homogeneously expanding wind with density profile $n \propto r^{-2}$ lying above an opaque emitting surface at velocity coordinate 100 km s^{-1} . The wind extended to $2,000 \text{ km s}^{-1}$ and the Sobolev optical depth had values of $\tau = 1$ (black lines), $\tau = 10$ (red lines), and $\tau = 100$ (blue lines). Discrepancies in the $\tau = 100$ case are likely due to the breakdown of the Sobolev approximation (§ 5.1.1) at high optical depth.

cally thin, and the dust opacity was assumed to be wavelength independent and completely absorbing (§ 2.4). Because of the relatively low optical depths encountered in these models, no “core-skipping” scheme was applied to accelerate the resonant line transport, and recoil effects were ignored.

In a resonant line interaction, a photon excites an atom from the ground state to an excited level. The end result is either scattering (i.e., de-excitation back to the ground state) or fluorescence (de-excitation to another excited level). The probability that the atom de-excites to lower level x is $p_{ux} = A_{ux} / \sum_i A_{ui}$, where the A_{ui} are the Einstein spontaneous emission coefficients and the sum runs over all levels accessible from the upper state u . For each interaction event, a random number was drawn to sample the final state from this probability distribution. If the result was a scattering, the process was assumed to be coherent in the comoving frame. If the result was fluorescence, the packet was reemitted at the line center wavelength of the new transition. Natural line broadening in fluorescence was ignored given the high velocity gradients in our models. In all cases, the angular redistribution was assumed to be isotropic.

To generate multi-dimensional images and spectra of the system, an escape probability method was used. At the initiation of a packet, and at every subsequent interaction event, we calculated the probability $P_x = e^{-\tau_{ux}} p_{ux}$, that the packet de-excited into state x and escaped the domain in some pre-specified direction. Here τ_{ux} is the optical depth to infinity, which was constructed by integration along the path to escape, taking into account the relevant Doppler shifts and possible absorption by lines or dust. The contribution of the packet to the final spectrum was then added in for every possible final state, each shifted to the proper observer-frame wavelength and weighted by the probability P_x .

To validate the monte carlo code, we calculated a series of test problems consisting of a point source embedded in a spherical, homogenous medium of varying resonant line optical depth. The resulting resonant line profiles (see Kasen et al. 2010) were found to be in good agreement with the standard analytic solutions (Harrington 1973; Neufeld 1990; Dijkstra et al. 2006). As a further test, we calculated line profiles for the case of an extended spherical source embedded in a homologously expanding wind with large velocity gradient. These model spectra (Figure 2) are in good agreement with ones determined by direct numerical integration of the radiation transport equation under the Sobolev approximation (§ 5.1.1; e.g., Jeffery & Branch 1990).

2.4. Dust

For the majority of models studied in this paper, we assume the gas contains no dust. This is an invalid assumption, especially for material associated with the ISM of a galaxy. Essentially all astrophysical environments that contain both cool gas and metals also show signatures of dust depletion and extinction. This includes the ISM of star-forming and H I-selected galaxies (e.g. Savage & Sembach 1996; Prochaska & Wolfe 2001; Prochaska et al. 2007), strong Mg II metal-line absorption systems (York et al. 2006; Ménard et al. 2008), and the galactic winds traced by low-ion transitions (Pettini et al. 2002; Rupke et al. 2005b). Extraplanar material likely associated with a galactic-scale outflow has been observed to emit IR radiation characteristic of dust (e.g. Hughes et al. 1990; Alton et al. 1999; Radovich et al. 2001). In addition, Ménard et al. (2010) have argued from a statistical analysis that dust is distributed to many tens of kpc from $z \sim 0.1$ galaxies and have suggested it was transported from the galaxies by galactic-scale winds. Although the galactic winds traced specifically by Mg II and Fe II transitions have not (yet) been demonstrated to contain dust, it is reasonable to consider its effects.

For analysis on normalized spectra (i.e. absorption lines), the effects of dust are largely minimized; dust has a nearly constant opacity over small spectral regions and all features are simply scaled together. For scattered and resonantly trapped photons, however, the relative effect of dust extinction can be much greater. These photons travel a much longer distance to escape the medium and may experience a much higher integrated opacity from dust. Indeed, dust is frequently invoked to explain the weak (or absent) Ly α emission from star-forming galaxies (e.g. Shapley et al. 2003). Although the transitions studied here have much lower opacity than Ly α , dust could still play an important role in the predicted profiles.

In a few models, we include absorption by dust under the following assumptions: (i) the dust opacity scales with the density of the gas (i.e. we adopt a fixed dust-to-gas ratio); (ii) the opacity is independent of wavelength, a reasonable approximation given the small spectral range analyzed; (iii) dust absorbs but does not scatter photons; (iv) the photons absorbed by dust are re-emitted at IR wavelengths and are ‘lost’ from the system. The dust absorption is normalized by τ_{dust} , the integrated opacity of dust from the center of the system to infinity. The ambient ISM of a star-forming galaxy may be expected to exhibit τ_{dust} values of one to a few at $\lambda \sim 3000\text{\AA}$ (e.g.

Charlot & Fall 2000).

2.5. The Sobolev Approximation

A photon propagating through a differentially expanding medium interacts with a line only when its comoving frame wavelength is Doppler-shifted into near resonance with the line center rest wavelength. For a wind with a steep velocity law (i.e. a large gradient dv/dr) and/or a narrow intrinsic profile (i.e. a small Doppler parameter), the spatial extent of the region of resonance may be much smaller than the length scale of the wind itself. The interaction can then be considered to occur at a point. In this case, Sobolev (1960) introduced a formalism that gives the line optical depth $\tau(r)$ at a given point in terms of the density and velocity gradient of the flow at that radius. For a wind in homologous expansion, this optical depth is independent of the direction of propagation and is given by

$$\tau_S(r) = K_\ell \lambda_\ell^0 |dv/dr|^{-1} \quad , \quad (1)$$

where

$$K_\ell = \frac{\pi e^2}{m_e c} f_\ell n_\ell(r) \quad (2)$$

is the integrated line opacity, λ_ℓ^0 the line-center rest wavelength, f_ℓ the oscillator strength and n_ℓ the density in the lower level of the transition. We have neglected corrections for stimulated emission. This optical depth applies to a photon with wavelength $\lambda_S \equiv \lambda_\ell(1 - v(r) \cdot \hat{r} \cdot \hat{d}/c)$ where \hat{d} is the direction of propagation. The probability that such a photon is scattered/absorbed at the point of resonance is simply $1 - \exp[-\tau_S(r)]$. We find that the Sobolev approximation applies for nearly all of the models presented in this paper, and therefore provides a convenient approach to estimating the optical depth.

3. THE FIDUCIAL WIND MODEL

In this section, we study a simple yet illustrative wind model for a galactic-scale outflow. The properties of this wind were tuned, in part, to yield a Mg II absorption profile similar to those observed for $z \sim 1$, star-forming galaxies (Weiner et al. 2009; Rubin et al. 2010a). We emphasize, however, that we do not favor this fiducial model over any other wind scenario nor do its properties have special physical motivation. Its role is to establish a baseline for discussion.

The fiducial wind is isotropic, dust-free, and extends from an inner wind radius r_{inner} to an outer wind radius r_{outer} . It follows a density law,

$$n_H(r) = n_H^0 \left(\frac{r_{\text{inner}}}{r} \right)^2 \quad , \quad (3)$$

and a velocity law with a purely radial flow

$$\vec{v} = v_r(r) \hat{r} = \frac{v_0 r}{r_{\text{outer}}} \hat{r} \quad . \quad (4)$$

For the fiducial case, the hydrogen density at the inner radius is $n_H^0 = 0.1 \text{ cm}^{-3}$ and the velocity at the outer radius is $v_0 = 1,000 \text{ km s}^{-1}$. Turbulent motions are characterized by a Doppler parameter⁷ $b_{\text{turb}} = 15 \text{ km s}^{-1}$.

⁷ The adopted Doppler parameter has a minor impact on the

TABLE 2
WIND PARAMETERS: FIDUCIAL MODEL

Property	Parameter	Value
Density law	$n(r)$	$\propto r^{-2}$
Velocity law	v_r	$\propto r$
Inner Radius	r_{inner}	1 kpc
Outer Radius	r_{outer}	20 kpc
Source size	r_{source}	0.5 kpc
Density Normalization	n_{H}^0	0.1 cm^{-3} at r_{inner}
Velocity Normalization	v_0	1000 km s^{-1} at r_{outer}
Turbulence	b_{turb}	15 km s^{-1}
Mg ⁺ Normalization	n_{Mg^+}	$10^{-5.47} n_{\text{H}}$
Fe ⁺ Normalization	n_{Fe^+}	$n_{\text{Mg}^+}/2$

We convert the hydrogen density n_{H} to the number densities of Mg⁺ and Fe⁺ ions by assuming solar relative abundances with an absolute metallicity of 1/2 solar and depletion factors of 1/10 and 1/20 for Mg and Fe respectively, i.e. $n_{\text{Mg}^+} = 10^{-5.47} n_{\text{H}}$ and $n_{\text{Fe}^+} = n_{\text{Mg}^+}/2$. At the center of the wind is a homogeneous source of continuum photons with size r_{source} . The parameters for the fiducial wind model are summarized in Table 2.

In Figure 3 we plot the density and velocity laws against radius; their simple power-law expressions are evident. The figure also shows the optical depth profile for the Mg II $\lambda 2796$ transition (τ_{2796}), estimated from the Sobolev approximation⁸ (Equation 1). The τ_{2796} profile peaks with $\tau_{2796}^{\text{max}} \approx 30$ at a velocity $v_r \approx 65 \text{ km s}^{-1}$ corresponding to $r \approx 1.3 r_{\text{inner}}$. The optical depth profile for the Mg II $\lambda 2803$ transition (not plotted) is scaled down by the $f\lambda$ ratio but is otherwise identical. Similarly, the optical depth profiles for the Fe II $\lambda\lambda 2586, 2600$ transitions are scaled down by $f\lambda$ and the $n_{\text{Fe}^+}/n_{\text{Mg}^+}$ ratio.

For the spatially integrated (i.e., 1D) spectra, the actual dimensions and density of the wind are unimportant provided they scale together to give nearly the same optical depth. Therefore, one may consider the choices for r_{inner} , r_{outer} , and n_{H}^0 as largely arbitrary. Nevertheless, we adopted values for this fiducial model with some astrophysical motivation, e.g., values that correspond to galactic dimensions and a normalization that gives $\tau_{2796}^{\text{max}} \sim 10$.

Using the methodology described in § 2, we propagated photons from the source and through the outflow to an ‘observer’ at $r \gg r_{\text{outer}}$ who views the entire wind+source complex. Figure 4 presents the 1D spectrum that this observer would record, with the unattenuated flux normalized to unit value. The Mg II doublet shows the canonical ‘P-Cygni profile’ that characterizes a continuum source embedded within an outflow. Strong absorption is evident at $\delta v \equiv (\lambda/\lambda_0 - 1) < -50 \text{ km s}^{-1}$ in both transitions (with equivalent widths $W_a^{2796} = 3.0 \text{ \AA}$ and $W_a^{2803} = 1.3 \text{ \AA}$) and each shows emission at positive velocities. For an isotropic and dust-free model, the total

results. The absorption profiles are insensitive to its value and varying b_{turb} only tends to modify the widths and modestly shift the centroids of emission lines.

⁸ We have verified this approximation holds by calculating τ_{2796} first as a function of velocity by summing the opacity for a series of discrete and small radial intervals between r_{inner} and r_{outer} . We then mapped τ_{2796} onto radius using the velocity law (Equation 4). This optical depth profile is shown as the black dotted line in Figure 3.

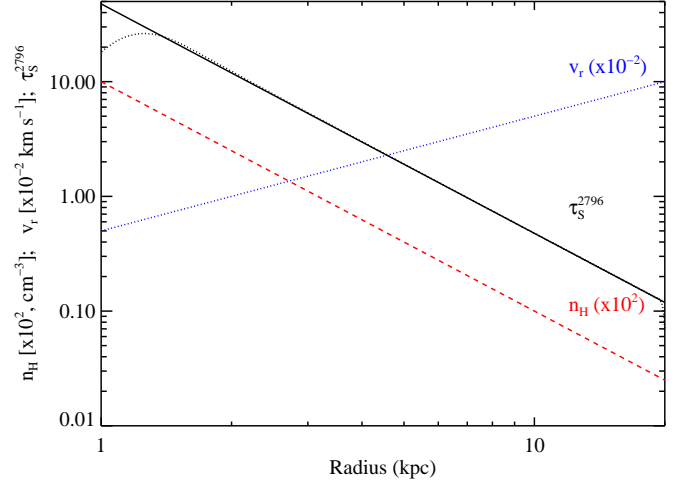


FIG. 3.— Density (dashed; red), radial velocity (dotted; blue), and Mg II $\lambda 2796$ optical depth profiles (solid and dotted; black) for the fiducial wind model (see Table 2 for details). The density and velocity laws are simple r^{-2} and r^1 power-laws; these curves have been scaled for plotting convenience. The optical depth profile was calculated two ways: (i) using the Sobolev approximation (Equation 1; solid black curve) and (ii) summing the opacity at small and discrete radial intervals in velocity space and then converting to radius with the velocity law (dotted black curve). These give very similar results. The wind parameters were set to give an optically thick medium at the inner radius ($r_{\text{inner}} = 1 \text{ kpc}$) that becomes optically thin at the outer radius ($r_{\text{outer}} = 20 \text{ kpc}$).

TABLE 3
EQUIVALENT WIDTHS FOR THE FIDUCIAL MODEL

Transition	v_{int}^a (km s^{-1})	W_{λ}^b (\AA)
MgII 2796	[−1030, −65]	2.96
	[−65, 311]	−1.75
MgII 2803	[−458, −57]	1.29
	[−57, 692]	−2.34
FeII 2586	[−365, −46]	0.59
	[−46, 186]	−0.10
FeII 2600	[−626, −78]	1.16
	[−49, 470]	−0.94
FeII* 2612	[−219, 183]	−0.33
FeII* 2626	[−194, 177]	−0.27
FeII* 2632	[−155, 130]	−0.16

^a Velocity interval over which the equivalent width is calculated.

^b Negative values indicate line-emission.

equivalent width of the doublet must be zero, i.e. every photon absorbed eventually escapes the system, typically at lower energy. The wind simply shuffles the photons in frequency space. A simple summation of the absorption and emission equivalent widths (Table 3) confirms this expectation.

Focusing further on the Mg II absorption, one notes that the profiles lie well above zero intensity and have similar depth even though their $f\lambda$ values differ by a factor of two. In standard absorption-line analysis, this is the tell-tale signature of a ‘cloud’ that has a high optical depth (i.e. is saturated) which only partially covers the emitting source (e.g. Rupke et al. 2005a; Hamann et al.

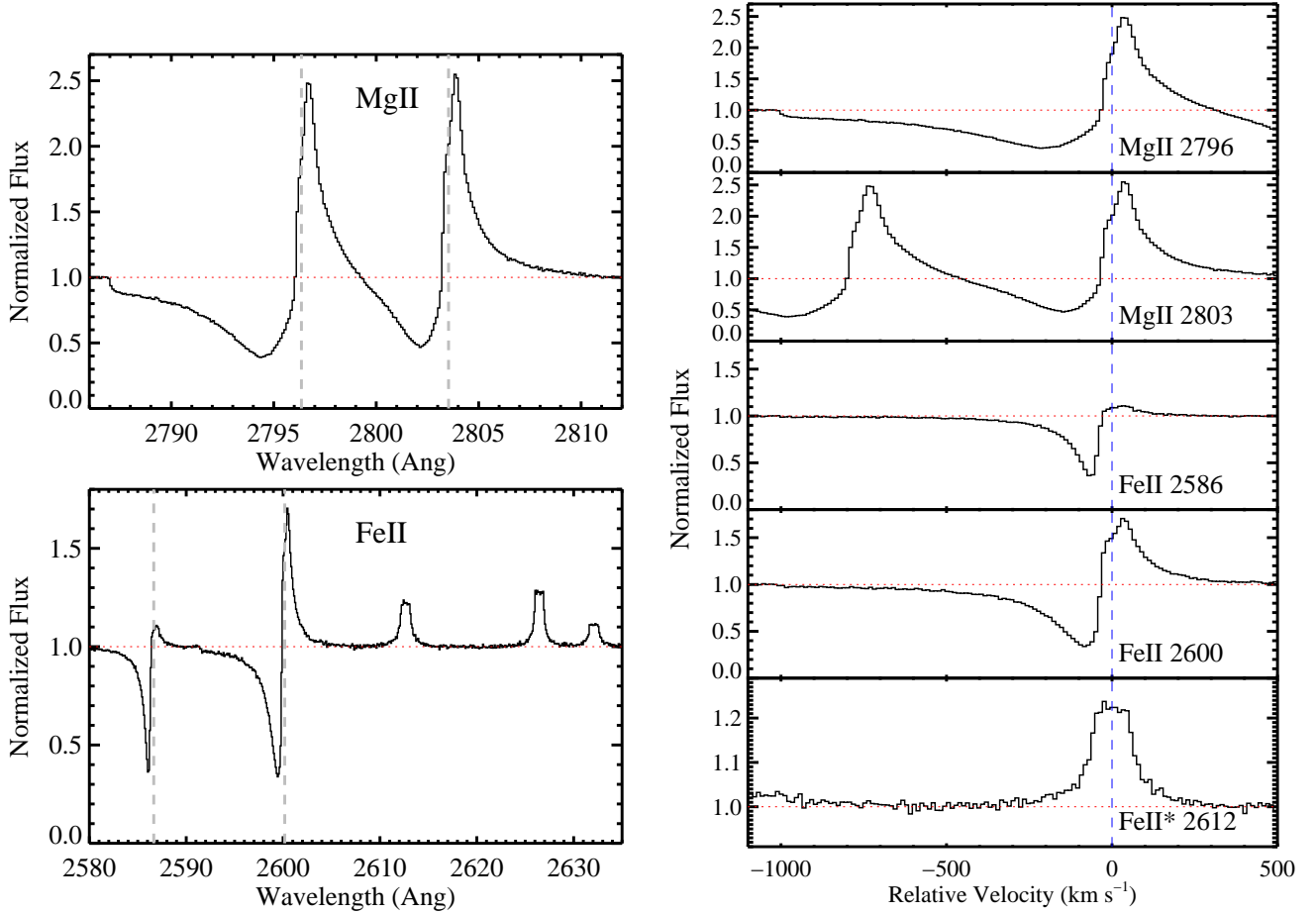


FIG. 4.— *Left* – (Upper) Mg II $\lambda\lambda 2796, 2803$ profiles for the fiducial wind model described in Table 2 and Figure 3. The doublet shows the P-Cygni profiles characteristic of an outflow with significant absorption blueward of line-center (dashed vertical lines) extending to $v = -1000$ km s $^{-1}$ and significant emission redward of line-center. Note that even though the peak optical depth of the Mg II transitions is $\tau_{2796}^{\max} \approx 30$ at $v \approx -70$ km s $^{-1}$, photons scattered off the outflow significantly fill-in the absorption. (Lower) Fe II absorption and emission profiles for the UV1 multiplet at $\lambda \approx 2600$ Å. The Fe II $\lambda\lambda 2586, 2600$ resonance lines show weaker absorption due to the smaller Fe $^{+}$ number density and lower $f\lambda$ values. Each also shows a P-Cygni profile, although the emission for Fe II $\lambda 2586$ is much weaker than that for the Fe II $\lambda 2600$ and Mg II $\lambda\lambda 2796, 2803$ transitions. This is because a majority of the absorbed Fe II $\lambda 2586$ photons fluoresce into Fe II* $\lambda\lambda 2612, 2632$ photons. *Right* – A subset of the transitions displayed in a velocity plot.

2010). Our fiducial wind model, however, *entirely covers the source*; the apparent partial covering must be related to a different effect. Figure 5 further emphasizes this point by comparing the absorption profiles from Figure 4 against an artificial model where no absorbed photons are re-emitted. As expected from the τ_{2796} profile (Figure 3), this ‘intrinsic’ model produces a strong Mg II $\lambda\lambda 2796, 2803$ doublet that absorbs all photons at $\delta v \approx -100$ km s $^{-1}$, i.e. $I_{2796}^{\min} = \exp(-\tau_{2796}^{\max}) \approx 0$. The true model, in contrast, has been ‘filled in’ at $\delta v \approx -100$ km s $^{-1}$ by photons scattered in the wind. An absorption-line analysis that ignores these effects would (i) systematically underestimate the true optical depth and/or (ii) falsely conclude that the wind partially covers the source. We will find that these are generic results, even for wind models that include dust and are not fully isotropic.

Turning to the emission profiles of the Mg II $\lambda\lambda 2796, 2803$ doublet, one notes that they are quite similar with comparable equivalent widths.

This is because the gas is optically thick yielding comparable total absorption. The flux of the Mg II $\lambda 2803$ transition even exceeds that for Mg II $\lambda 2796$ because the wind speed is greater than the velocity separation of the doublet, $|v_r|_{\max} > (\Delta v)_{\text{MgII}}$. Therefore, the red wing of the Mg II $\lambda 2796$ emission profile is partially absorbed by Mg II $\lambda 2803$ and re-emitted at lower frequency. This yields a line ratio that is far below the 2 : 1 ratio that one may have naively expected (e.g. if the line-emission resulted from recombinations), and leads us to conclude that the relative strengths of the emission lines are sensitive to both the opacity and velocity extent of the wind.

Now consider the Fe II transitions: the bottom left panel of Figure 4 covers the majority of the Fe II UV1 transitions and several are shown in the velocity plot. The line profile for Fe II $\lambda 2600$ is very similar to the Mg II $\lambda\lambda 2796, 2803$ doublet; one observes strong absorption to negative velocities and strong emission at $\delta v > 0$ km s $^{-1}$ producing a characteristic P-Cygni pro-

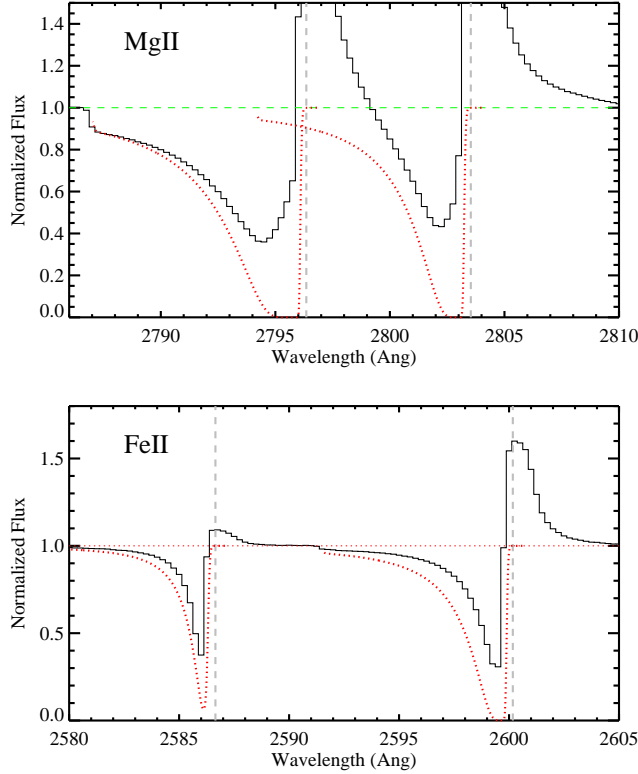


FIG. 5.— The solid curves show the line profiles (absorption and emission) of the Mg II and Fe II resonance lines for the fiducial wind model. These include the effects of scattered photons and show the canonical P-Cygni profiles of a source embedded within an outflow. Overplotted on each transition (dotted red line) is the predicted absorption profile under the constraint that every absorbed photon is lost from the system (referred to as the intrinsic profile), i.e. no scattering or re-emission occurs. The intrinsic profiles have been ‘filled-in’ significantly with photons scattered by the wind into our sightline. Ignoring this process, one would model the absorption lines with a systematically lower optical depth and/or (incorrectly) conclude that the source is partly covered by the gas.

file. Splitting the profile at $\delta v = -50 \text{ km s}^{-1}$, we measure an equivalent width $W_a^{2600} = 1.16 \text{ \AA}$ in absorption and $W_e^{2600} = -0.94 \text{ \AA}$ in emission (Table 3) for a total equivalent width of $W_{\text{TOT}}^{2600} \approx 0.22 \text{ \AA}$. In contrast, the Fe II $\lambda 2586$ resonance line shows much weaker emission and a much higher total equivalent width ($W_{\text{TOT}}^{2586} = 0.49 \text{ \AA}$), even though the line has a $2\times$ lower $f\lambda$ value. These differences between the Fe II resonance lines (and between Fe II and Mg II) occur because of the complex of non-resonant Fe II* transitions that are coupled to the resonance lines (Figure 1). Specifically, a resonance photon absorbed at Fe II $\lambda\lambda 2586, 2600$ has a finite probability of being re-emitted as a non-resonant photon which then escapes the system without further interaction. The principal effects are to reduce the line emission of Fe II $\lambda\lambda 2586, 2600$ and to produce non-resonant line-emission (e.g. Fe II* $\lambda 2612$).

The reduced Fe II $\lambda 2586$ emission relative to Fe II $\lambda 2600$ is related to two factors: (i) there is an additional downward transition from the $z \text{ } ^6\text{D}^0_{7/2}$ level and (ii) the Einstein A coefficients of the non-resonant lines coupled to Fe II $\lambda 2586$ are comparable to and even exceed the Einstein A coefficient of the resonant transition. In contrast, the Fe II* $\lambda 2626$ transition (associated with

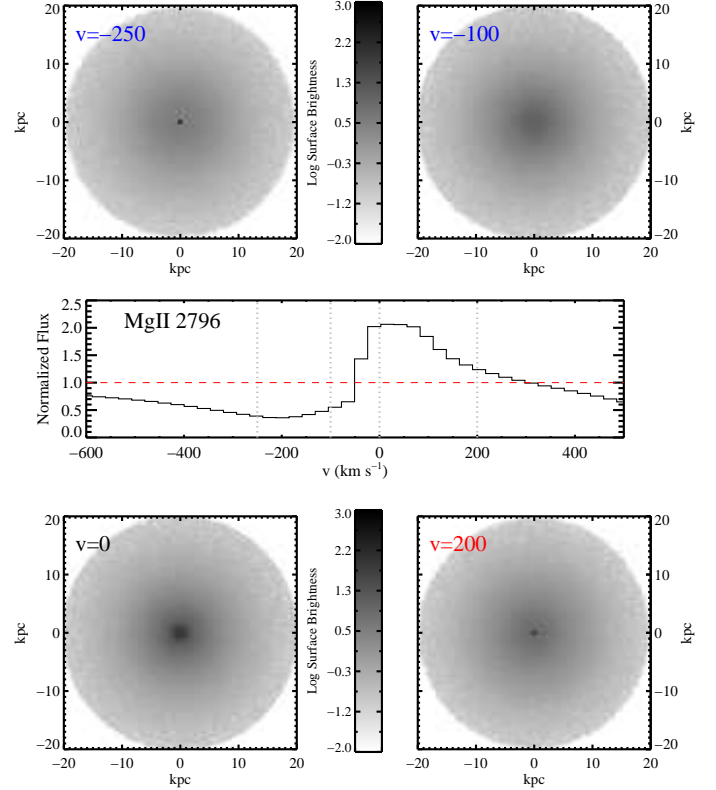


FIG. 6.— Surface-brightness emission maps around the Mg II $\lambda 2796$ transition for the source+wind complex of the fiducial model. The middle panel shows the 1D spectrum with $v = 0 \text{ km s}^{-1}$ corresponding to $\lambda = 2796.35 \text{ \AA}$ and the dotted vertical curves indicate the velocity slices for the emission maps. The source has a size $r_{\text{source}} = 0.5 \text{ kpc}$, traced by a few pixels at the center of each map. At $v = -250 \text{ km s}^{-1}$, the wind has an optical depth of $\tau_{2796} \approx 1$ and the source contributes roughly half of the observed flux. At $v = -100 \text{ km s}^{-1}$ the wind absorbs all photons from the source and the observed emission is entirely due to photons scattered by the wind. Amazingly, this emission exceeds the integrated flux at $v = -250 \text{ km s}^{-1}$ such that the Mg II $\lambda 2796$ line center is offset from the (intrinsic) peak in optical depth. At $v \geq 0 \text{ km s}^{-1}$, both the source and wind contribute to the observed emission. At all velocities, the majority of emission comes from the inner $\approx 5 \text{ kpc}$.

Fe II $\lambda 2600$) has an approximately $4\times$ smaller A coefficient than the corresponding resonance line. Therefore, the majority of photons absorbed at $\lambda \approx 2600 \text{ \AA}$ are re-emitted as Fe II $\lambda 2600$ photons, whereas the majority of photons absorbed at $\lambda \approx 2586 \text{ \AA}$ are re-emitted at longer wavelengths (Fe II* $\lambda 2612$ or $\lambda 2632$). If we increase τ_{2600} (and especially if we include gas with $v_r \approx 0 \text{ km s}^{-1}$) then the Fe II $\lambda 2600$ emission is significantly suppressed (e.g. § 4.3). The total equivalent width, however, of the three lines connected to the $z \text{ } ^6\text{D}^0_{7/2}$ upper level must still vanish (photons are conserved in this isotropic, dust-free model).

The preceding discussion emphasizes the filling-in of resonance absorption at $\delta v \lesssim -50 \text{ km s}^{-1}$ and the generation of emission lines at $\delta v \approx 0 \text{ km s}^{-1}$ by photons scattered in the wind. We also mapped the emission of the fiducial model to study its spatial extent (see § 2.3 for a description of the algorithm). The output is a set of surface-brightness maps in a series of frequency channels yielding a dataset analogous to integral-field-unit (IFU)

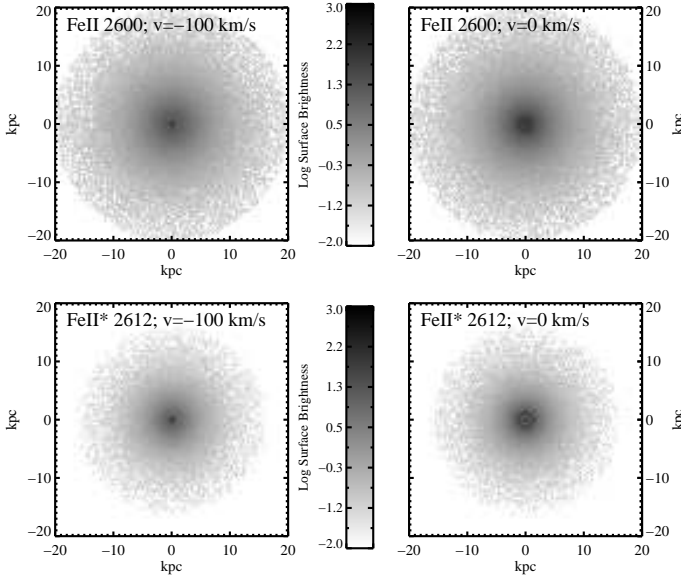


FIG. 7.— (Upper) Surface-brightness emission maps around the Fe II $\lambda 2600$ transition for the source+wind complex. The results are very similar to those observed for the Mg II $\lambda\lambda 2796, 2803$ doublet (Figure 6). (Lower) Surface-brightness emission maps around the Fe II $\lambda 2612$ transition for the source+wind complex. In this case, the source is unattenuated yet scattered photons from the wind also make a significant contribution.

observations. In Figure 6, we present the output at several velocities relative to the Mg II $\lambda 2796$ transition. At $\delta v = -250 \text{ km s}^{-1}$, where the wind has an optical depth $\tau_{2796} < 1$ (Figure 3), the source contributes roughly half of the observed flux. At $\delta v = -100 \text{ km s}^{-1}$, however, the wind absorbs all photons from the source and the observed emission is entirely from photons scattered by the wind. This scattered emission actually exceeds the source+wind emission at $\delta v = -250 \text{ km s}^{-1}$ such that the absorption profile is negatively offset from the velocity where τ_{2796} is maximal (Figure 3). The net result is weaker Mg II absorption that peaks blueward of the actual peak in the optical depth profile. Table 4 reports several kinematic measurements of the absorption and emission features. Clearly, these effects complicate estimates for the speed, covering fraction, and total column density of the wind. At $\delta v = 0 \text{ km s}^{-1}$, the wind and source have comparable total flux with the latter dominating at higher velocities.

Similar results are observed for the Fe II resonance transitions (Figure 7). For transitions to fine-structure levels of the a^6D^0 configuration, the source is unattenuated but there is a significant contribution from photons generated in the wind.

At all velocities, the majority of light comes from the inner regions of the wind. The majority of Mg II emission occurs within the inner few kpc, e.g. 50–60% of the light at $\delta v = -100$ to $+100 \text{ km s}^{-1}$ comes from $|r| < 3 \text{ kpc}$. The emission is even more centrally concentrated for the Fe II transitions. A proper treatment of these distributions is critical for interpreting observations acquired through a slit, i.e. where the aperture has a limited extent in one or more dimensions. A standard longslit on 10m-class telescopes, for example, subtends $\approx 1''$ corresponding to 5–10 kpc for $z \sim 1$. We return to this issue

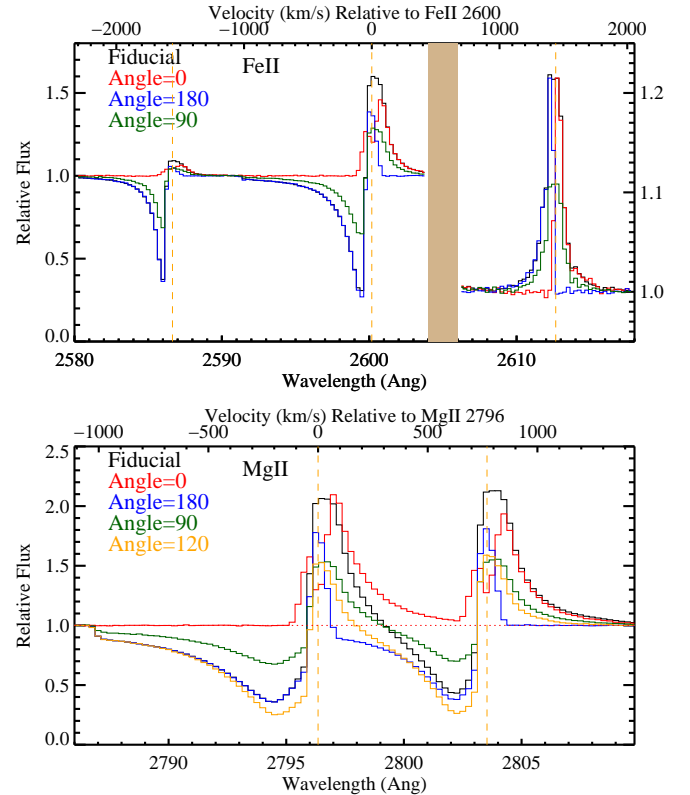


FIG. 8.— Profiles of the Fe II and Mg II profiles for the fiducial case (black lines) compared against an anisotropic wind blowing into only 2π steradians as viewed from $\phi = 0^\circ$ (source uncovered) to $\phi = 180^\circ$ (source covered). One detects significant emission for all orientations but significant absorption only for $\phi \geq 90^\circ$. The velocity centroid of the emission shifts from positive to negative velocities as ϕ increases and one transitions from viewing the wind as lying behind the source to in front of it. The velocity centroid of emission, therefore, diagnoses the degree of anisotropy for the wind.

in § 6.

The results presented in Figures 6 and 7 are sensitive to the radial extent, morphology, density and velocity profiles of this galactic-scale wind. Consequently, IFU observations of line emission from low-ion transitions may offer the most direct constraints on galactic-scale wind properties.

4. VARIATIONS TO THE FIDUCIAL MODEL

In this section, we investigate a series of more complex wind scenarios through modifications to the fiducial model. These include relaxing the assumption of isotropy, introducing dust, adding an ISM component within r_{inner} , and varying the normalization of the optical depth profiles.

4.1. Anisotropic Winds

The fiducial model assumes an isotropic wind with only radial variations in velocity and density. Angular isotropy is obviously an idealized case, but it is frequently assumed in studies of galactic-scale outflows (e.g. Steidel et al. 2010). There are several reasons, however, to consider anisotropic winds. Firstly, galaxies are not spherically symmetric; the sources driving the wind (e.g. supernovae, AGN) are very unlikely to be spherically distributed within the galaxy. Secondly, the galactic ISM

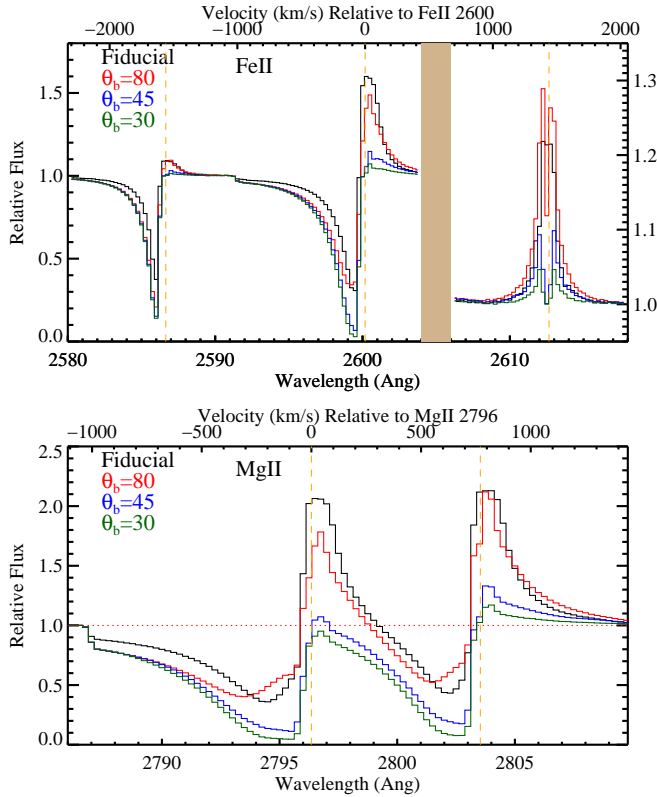


FIG. 9.— Profiles of the Fe II and Mg II profiles for the fiducial case (black lines) compared against a bi-conical wind with varying opening angle ($\theta_b = 0^\circ$ is a full wind). For modest angles, one observes similar results to the fiducial model but larger angles ($\theta_b > 45^\circ$) the emission is significantly suppressed at all velocities.

frequently has a disk-like morphology which will suppress the wind preferentially at low galactic latitudes, perhaps yielding a bi-conic morphology (e.g. Heckman et al. 1990; Walter et al. 2002). Lastly, the galaxy could be surrounded by an aspherical gaseous halo whose interaction would produce an irregular outflow.

With these considerations in mind, we reanalyzed the fiducial model with the 3D algorithm after departing from isotropy. It is beyond the scope of this paper to explore a full suite of anisotropic profiles. We consider two simple examples: (i) half the fiducial model, where the wind density is set to zero for 2π steradians (i.e. a hemispherical wind). This model is viewed from $\phi = 0^\circ$ (source uncovered) to $\phi = 180^\circ$ (source covered); and (ii) a bi-conical wind which fills $|\theta| < \theta_b$ both into and out of the plane of the sky and that is viewed along the axis of rotational symmetry ($\theta = 0^\circ$ is defined along this axis).

The resulting Mg II and Fe II profiles for the half wind are compared against the fiducial model (isotropic wind) in Figure 8. Examining the Mg II $\lambda\lambda 2796, 2803$ doublet, the $\phi = 0^\circ$ model only shows line-emission from photons scattered off the back side. These photons, by definition, have $\delta v \gtrsim 0 \text{ km s}^{-1}$ relative to line-center (a subset have $\delta v \lesssim 0 \text{ km s}^{-1}$ because of turbulent motions in the wind). When viewed from the opposite direction ($\phi = 180^\circ$), the absorption lines dominate, but there is still significant line-emission at $\delta v \approx 0 \text{ km s}^{-1}$ and at $\delta v < 0 \text{ km s}^{-1}$ from photons that scatter through the wind which fills in the absorption. The key difference between this and the isotropic wind is the absence of photons scattered to

$\delta v > 100 \text{ km s}^{-1}$; this also implies deeper Mg II $\lambda 2803$ absorption at $\delta v \approx -100 \text{ km s}^{-1}$. The shifts in velocity centroid and asymmetry of the emission lines serve to diagnose the degree of wind isotropy, especially in conjunction with analysis of the absorption profiles. The results are similar for the Fe II $\lambda\lambda 2586, 2600$ resonance lines. The Fe II* $\lambda 2612$ line, meanwhile, shows most clearly the offset in velocity between the source unobscured ($\phi = 0^\circ$) and source covered ($\phi = 180^\circ$) cases. The offset of the Fe II* lines is the most significant difference from the fully isotropic wind.

We have also analyzed the predicted profiles for a series of bi-conical winds with $\theta_b = 30 - 80^\circ$, each viewed along the axis of rotational asymmetry with the wind covering the source. Figure 9 and Table 4 summarizes the results for several cases. For $\theta_b = 80^\circ$, the results are very similar to the fiducial model; the profiles show similar equivalent widths for absorption and emission. The key quantitative difference is that the Fe II* line-emission is modestly suppressed at $\delta v \approx 0 \text{ km s}^{-1}$ because the portion of the wind with that projected velocity has been removed. For more highly collimated winds $\theta_b < 45^\circ$, however, the line-emission is several times weaker than the fiducial model. Similarly, the absorption-line profiles more closely track the intrinsic optical depth of the outflow. Of course, these same models when viewed ‘side-ways’ would show no absorption but strong line-emission. Such events are sufficiently rare (Rubin et al., in prep) that we consider this level of anisotropy to be uncommon. Nevertheless, the results for a bi-conic clearly have important implications for the nature of absorption and line-emission in our fiducial model.

4.2. Dust

As described in § 2.4, one generally expects dust in astrophysical environments that contain cool gas and metals. This dust modifies the observed wind profiles in two ways. First, it is a source of opacity for all of the photons. This suppresses the flux at all wavelengths by $\approx \exp(-\tau_{\text{dust}})$ but because we re-normalize the profiles, this effect is essentially ignored. Second, photons that are scattered by the wind must travel a greater distance to escape and therefore suffer from greater extinction. A photon that is trapped for many scatterings has an increased probability of being absorbed by dust. Section 2.4 describes the details of our treatment of dust; we remind the reader here that we assume a constant dust-to-gas ratio that is normalized by the total optical depth τ_{dust} photons would experience if they traveled from the source to infinity without scattering.

In Figure 10, we show the Mg II and Fe II profiles of the fiducial model ($\tau_{\text{dust}} = 0$) against a series of models with $\tau_{\text{dust}} > 0$. For the Mg II transitions, the dominant effect is the suppression of line emission at $\delta v \geq 0 \text{ km s}^{-1}$. These ‘red’ photons have scattered off the backside of the wind and must travel a longer path than other photons. Dust leads to a differential reddening that increases with velocity relative to line-center. This is a natural consequence of dust extinction and is most evident in the Fe II* $\lambda 2612$ emission profile which is symmetrically distributed around $\delta v = 0 \text{ km s}^{-1}$ in the $\tau_{\text{dust}} = 0$ model. The degree of suppression of the line-emission is relatively modest, however. Specifically, we find that the flux is reduced by a factor of the order of $(1 + \tau_{\text{dust}})^{-1}$

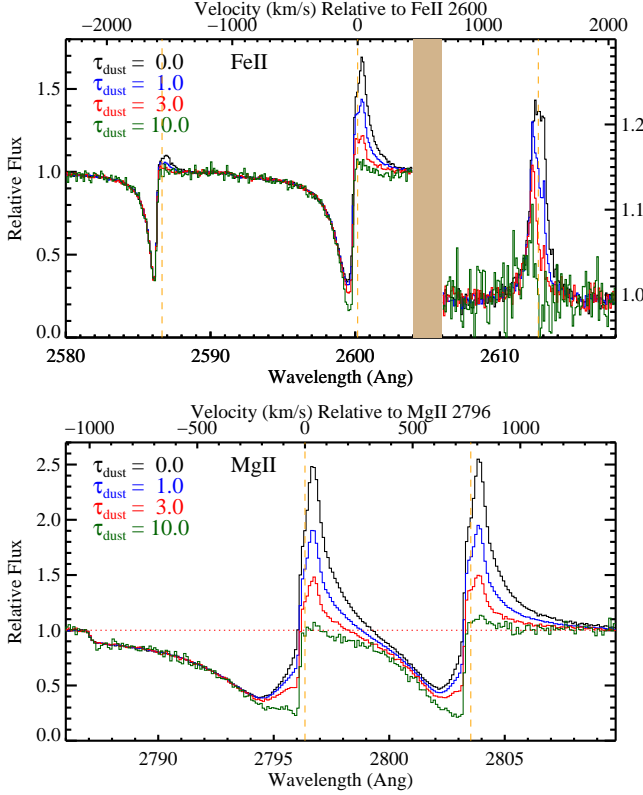


FIG. 10.— Profiles of the Fe II and Mg II profiles for the fiducial model (black) compared against a series of models that include dust extinction, parameterize by the integrated dust opacity from source to infinity (τ_{dust}). The primary effect of dust is to suppress the line-emission relative to the continuum. A more subtle but important effect is that the redder photons in the emission lines (corresponding to positive velocity offsets relative to line-center) suffer greater extinction. This occurs because the ‘redder’ photons that we view have travelled farther to scatter off the backside of the wind. Note that the absorption lines are nearly unmodified until $\tau_{\text{dust}} = 10$, a level of extinction that would preclude observing the source altogether.

(Figure 11), instead of the factor $\exp(-\tau_{\text{dust}})$ that one may have naively predicted. In terms of absorption, the profiles are nearly identical for $\tau_{\text{dust}} \leq 3$. One requires very high extinction to produce a deepening of the profiles at $\delta v \approx -100 \text{ km s}^{-1}$.

We conclude that dust has only a modest influence on this fiducial model and, by inference, on models with moderate peak optical depths and significant velocity gradients with radius (i.e. scenarios in which the photons scatter only one to a few times before exiting). For qualitative changes, one requires an extreme level of extinction ($\tau_{\text{dust}} = 10$). In this case, the source would be extinguished by 15 magnitudes and could never be observed. Even $\tau_{\text{dust}} = 3$ is larger than typically inferred for the star-forming galaxies that drive outflows (e.g. Charlot & Fall 2000). For the emission lines, the dominant effect is a reduction in the flux with a greater extinction at higher velocities relative to line-center. In these respects, dust extinction crudely mimics the behavior of the anisotropic wind described in Section 4.1.

4.3. ISM

The fiducial model does not include gas associated with the ISM of the galaxy, i.e. material at $r \sim 0 \text{ kpc}$ with $v_r \approx 0 \text{ km s}^{-1}$. This allowed us to focus on re-

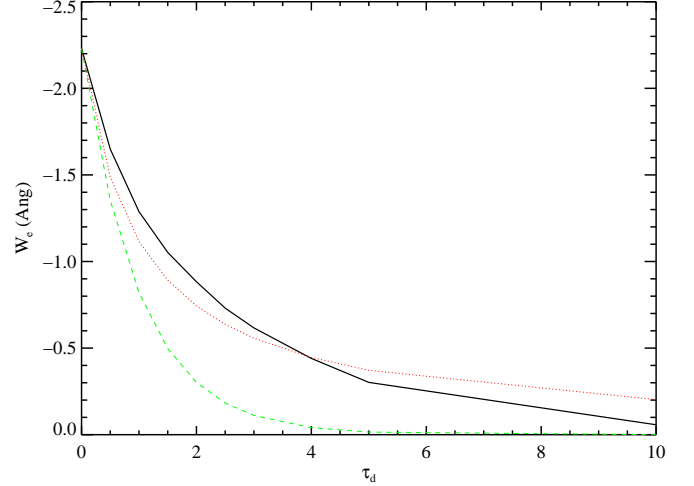


FIG. 11.— Predicted equivalent widths for Mg II $\lambda 2803$ line-emission from the fiducial wind model, as attenuated by dust with a range of τ_{dust} values. The black (solid) curve shows the model results. The dashed (green) curve shows $W_e(\tau_d) = W_e(\tau_d = 0) \cdot \exp(-\tau_d)$. It is obvious that the equivalent widths (i.e., the flux relative to the continuum) do not follow this scaling. The dotted (red) line, meanwhile, plots $W_e(\tau_d) = W_e(\tau_d = 0) \cdot (1 + \tau_d)^{-1}$. This simple approximation is a good representation of the results for our radiative transfer calculations.

sults related solely to a wind component. The decision to ignore the ISM was also motivated by the general absence of significant absorption at $\delta v \approx 0 \text{ km s}^{-1}$ in galaxies that exhibit outflows (e.g. Weiner et al. 2009; Rubin et al. 2010b; Steidel et al. 2010). On the other hand, the stars that comprise the source are very likely embedded within and fueled by gas from the ISM. Consider, then, a modification to the fiducial model that includes an ISM. Specifically, we assume the ISM component has density $n_H = 1 \text{ cm}^{-3}$ for $r_{\text{ISM}} \leq r < r_{\text{inner}}$ with $r_{\text{ISM}} = 0.5 \text{ kpc}$, an average velocity of $v_r = 0 \text{ km s}^{-1}$, and a larger turbulent velocity $b_{\text{ISM}} = 40 \text{ km s}^{-1}$. The resultant optical depth profile τ_{2796} is identical to the fiducial model for $r > 2 \text{ kpc}$, has a slightly higher opacity at $r = 1 - 2 \text{ kpc}$, and has a very large opacity at $r = 0.5 - 1 \text{ kpc}$.

In Figure 12, the solid curves show the Mg II and Fe II profiles for the ISM+wind and fiducial models. In comparison, the dotted curve shows the intrinsic absorption profile for the ISM+wind model corresponding to the (unphysical) case where none of the absorbed photons are scattered or re-emitted. Focus first on the Mg II doublet. As expected, the dotted curve shows strong absorption at $\delta v \approx 0 \text{ km s}^{-1}$ and blueward. The full models, in contrast, show non-zero flux at these velocities and even a normalized flux exceeding unity at $\delta v \approx 0 \text{ km s}^{-1}$. In fact, the ISM+wind model is nearly identical to the fiducial model; the only quantitative difference is that the velocity centroids of the emission lines are shifted redward by $\approx +100 \text{ km s}^{-1}$. We have also examined the spatial distribution of emission from this model and find results qualitatively similar to the fiducial wind model (Figures 6 and 7).

There are, however, several qualitative differences for the Fe II transitions. First, the Fe II $\lambda 2586$ transition in the ISM+wind model shows much stronger absorption at $\delta v \approx 0$ to -100 km s^{-1} . In contrast to the Mg II

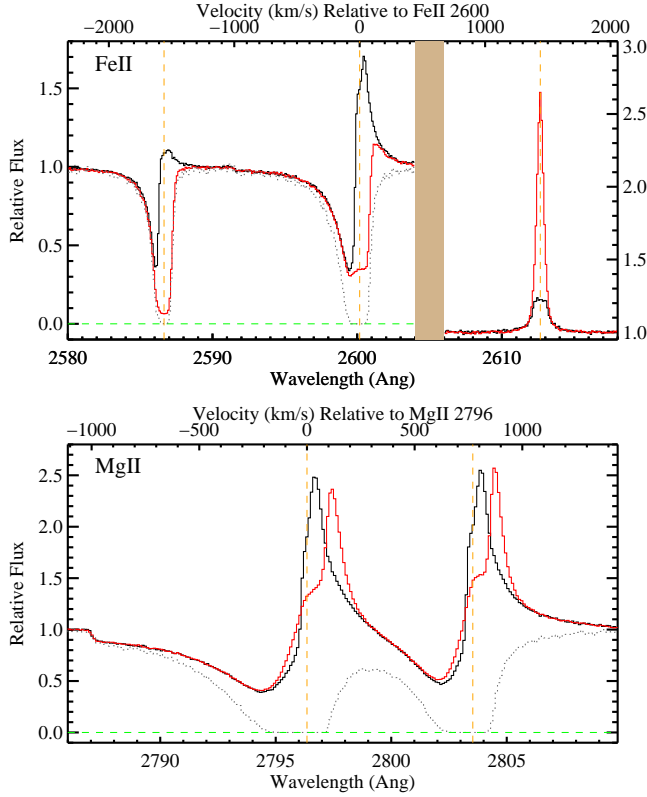


FIG. 12.— Profiles of the Fe II and Mg II profiles for the ISM+wind model (red) compared against the fiducial wind model (black). The dotted line traces the predicted absorption profile in the absence of re-emission and scattering. Regarding the Mg II doublet, the primary difference between the ISM+wind and the fiducial models is the shift of $\approx 100 \text{ km s}^{-1}$ in the emission lines from $v \approx 0 \text{ km s}^{-1}$ for the fiducial model to $v \approx +100 \text{ km s}^{-1}$ for the ISM+wind model. The Fe II profiles, meanwhile, show several qualitative differences. The Fe II $\lambda\lambda 2586, 2600$ resonance transitions each exhibit much greater absorption at $v \approx 0 \text{ km s}^{-1}$ than the fiducial model. The resonant line-emission is also substantially reduced, implying much higher fluxes for the non-resonant lines (e.g. Fe II* $\lambda 2612, 2626$). Lastly, we note that the Fe II $\lambda 2586$ absorption profile provides a good (albeit imperfect) representation of the wind opacity and therefore offers the best characterization of an ISM component.

doublet, the profile is not filled in by scattered photons. Instead, the majority of Fe II $\lambda 2586$ photons that are absorbed are re-emitted as Fe II* $\lambda\lambda 2612, 2632$ photons. In fact, the Fe II $\lambda 2586$ profile very nearly matches the profile without re-emission (compare to the dotted lines); this transition provides a very good description of the intrinsic ISM+wind optical depth profile. We conclude that resonant transitions that are coupled to (multiple) non-resonant, electric dipole transitions offer the best diagnosis of ISM absorption.

The differences in the Fe II absorption profiles are reflected in the much higher strengths ($3 - 10\times$) of emission from transitions to the excited states of the a^6D^0 configuration. This occurs because: (1) there is greater absorption by the Fe II $\lambda\lambda 2586, 2600$ resonance lines; and (2) the high opacity of the ISM component leads to an enhanced conversion of resonance photons with $\delta v \approx 0 \text{ km s}^{-1}$ into Fe II* photons. This is especially notable for the Fe II $\lambda 2600$ transition whose coupled Fe II* transition shows an equivalent width nearly $10\times$ stronger than for the fiducial model. The relative strengths of the

Fe II $\lambda 2600$ and Fe II* $\lambda 2626$ lines provide a direct diagnostic of the degree to which the resonance line photons are trapped, i.e. the peak optical depth of Fe II $\lambda 2600$ and the velocity gradient of the wind.

Because of the high degree of photon trapping within the ISM component, this model does suffer more from dust extinction than the fiducial model. We have studied the ISM+wind model including dust with $\tau_{\text{dust}} = 1$ (normalized to include the ISM gas). All of the emission lines are significantly reduced. The Mg II emission is affected most because these lines are resonantly trapped. The Fe II* emission is also reduced relative to the dust-free model, but the absolute flux still exceeds the fiducial model (Table 4). At large negative velocity offsets from systemic, the two profiles are nearly identical. We conclude that a dusty ISM model could show significant absorption at $\delta v \approx 0 \text{ km s}^{-1}$ in resonance lines (including Mg II) with strong line-emission in the Fe II* transitions.

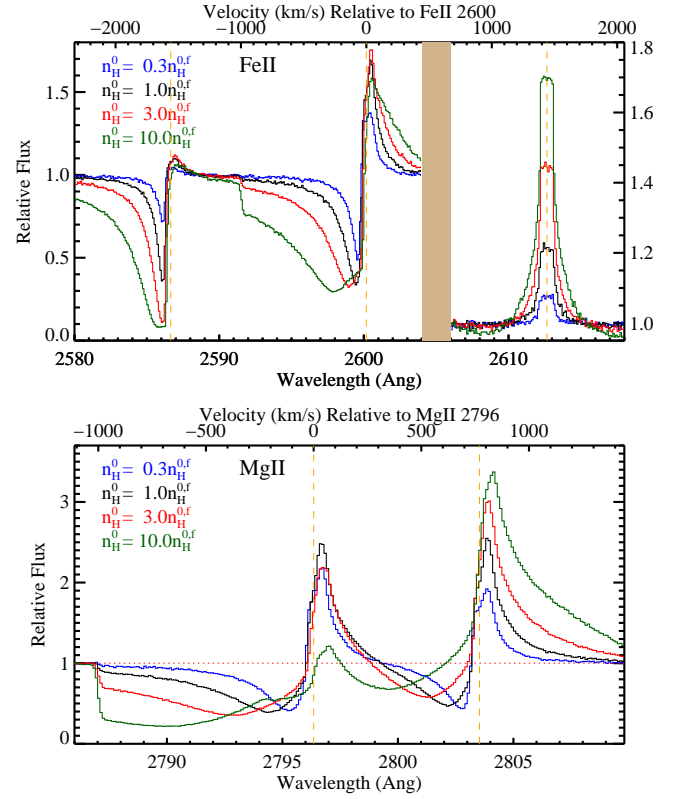


FIG. 13.— Mg II and Fe II profiles for the fiducial model with varying normalization, parameterized by n_{H}^0 . As expected, the strength of absorption increases with increasing n_{H}^0 ; this also results in stronger line-emission. Note that the Fe II $\lambda 2586$ emission is always weak. Only its absorption increases with n_{H}^0 and actually exceeds the depth of Fe II $\lambda 2600$ for $n_{\text{H}}^0 > n_{\text{H}}^{0,f}$. The depth of the Mg II doublet, meanwhile, always falls below a relative flux of 0.3 while the Mg II $\lambda 2803$ emission rises steadily with n_{H}^0 .

4.4. Varying n_{H}^0

The final modification to the fiducial model considered was a uniform variation of the normalization of the optical depth profiles. Specifically, we ran a series of additional models with n_{H}^0 at $1/3, 3,$ and 10 times the fiducial value of $n_{\text{H}}^{0,f} = 0.1 \text{ cm}^{-3}$. The resulting Mg II and Fe II

TABLE 4
LINE DIAGNOSTICS FOR THE FIDUCIAL MODEL AND VARIANTS

Transition	Model	v_{int}^a (km s ⁻¹)	W_i (Å)	W_a (Å)	τ_{pk}	v_τ (km s ⁻¹)	$v_{\bar{\tau}}$ (km s ⁻¹)	v_{int}^e (km s ⁻¹)	W_e (Å)	f_{pk}	v_f (km s ⁻¹)	$v_{\bar{f}}$ (km s ⁻¹)	Δv_e (km s ⁻¹)
MgII 2796	Fiducial	[-1009, -43]	4.78	2.83	0.94	-215	-372	[-32, 311]	-1.77	2.48	32	117	215
	$\phi = 0^\circ$	[-145, 606]	-2.34	2.10	70	208	483
	$\phi = 180^\circ$	[-1030, -65]	4.78	2.98	1.03	-199	-369	[-65, 70]	-0.51	1.78	-11	6	107
	$\theta_b = 80^\circ$	[-1030, -65]	4.78	3.55	0.91	-306	-442	[-65, 257]	-1.03	1.78	43	93	215
	$\theta_b = 45^\circ$	[-1003, -11]	4.78	4.79	2.19	-91	-332	[16, 96]	-0.04	1.07	43	55	54
	$\tau_{\text{dust}}=1$	[-1009, -32]	4.77	2.94	0.95	-215	-360	[-32, 257]	-0.95	1.90	32	101	193
	$\tau_{\text{dust}}=3$	[-998, -32]	4.78	3.07	1.03	-193	-342	[-22, 182]	-0.40	1.48	43	76	150
	ISM	[-1009, -65]	6.36	2.67	0.90	-204	-390	[-54, 311]	-1.60	2.36	118	125	236
	ISM+dust	[-998, 150]	6.42	4.06	1.06	-193	-270
MgII 2803	Fiducial	[-437, -41]	3.29	1.19	0.76	-148	-193	[-41, 676]	-2.24	2.55	34	269	449
	$\phi = 0^\circ$	[-84, 665]	-1.86	1.93	77	257	482
	$\phi = 180^\circ$	[-538, -57]	3.29	1.82	0.97	-137	-232	[-57, 104]	-0.59	1.81	-3	22	107
	$\theta_b = 80^\circ$	[-485, -57]	3.29	1.33	0.65	-217	-237	[-57, 746]	-2.30	2.12	23	303	535
	$\theta_b = 45^\circ$	[-538, -57]	3.29	2.60	1.74	-84	-217	[-30, 692]	-0.72	1.33	23	320	562
	$\tau_{\text{dust}}=1$	[-479, -41]	3.28	1.41	0.83	-137	-195	[-41, 591]	-1.30	1.95	34	247	417
	$\tau_{\text{dust}}=3$	[-533, -30]	3.26	1.67	0.94	-116	-195	[-30, 484]	-0.66	1.50	34	213	375
	ISM	[-426, -62]	6.49	1.03	0.67	-169	-206	[-51, 655]	-2.09	2.57	98	265	439
	ISM+dust	[-554, 130]	6.51	2.59	1.02	-137	-143	[173, 195]	-0.01	1.03	184	184	21
FeII 2586	Fiducial	[-348, -35]	0.82	0.61	1.01	-70	-119	[-35, 128]	-0.10	1.11	35	47	128
	$\phi = 0^\circ$	[-104, 186]	-0.10	1.06	70	41	232
	$\phi = 180^\circ$	[-365, -46]	0.82	0.60	1.01	-75	-133	[-46, 70]	-0.03	1.06	-17	12	87
	$\theta_b = 80^\circ$	[-481, -46]	0.82	0.96	1.57	-75	-148	[-46, 186]	-0.10	1.09	41	71	203
	$\theta_b = 45^\circ$	[-481, -46]	0.82	1.03	1.88	-75	-143	[41, 99]	-0.02	1.03	41	69	58
	$\tau_{\text{dust}}=1$	[-348, -35]	0.82	0.61	1.04	-70	-118	[-35, 116]	-0.05	1.06	23	41	116
	$\tau_{\text{dust}}=3$	[-313, -35]	0.94	0.60	1.06	-70	-113	[-23, 46]	-0.02	1.04	-12	12	58
	ISM	[-348, 104]	1.90	1.60	2.75	0	-29
	ISM+dust	[-313, 116]	1.84	1.63	2.96	23	-25	[278, 290]	-0.00	1.03	278	284	12
FeII 2600	Fiducial	[-580, -37]	1.87	1.18	1.08	-83	-181	[-37, 459]	-0.83	1.70	32	191	312
	$\phi = 0^\circ$	[-135, 442]	-0.78	1.46	67	144	346
	$\phi = 180^\circ$	[-597, -49]	1.87	1.18	1.31	-78	-188	[-49, 95]	-0.25	1.39	-20	22	87
	$\theta_b = 80^\circ$	[-856, -49]	1.87	1.72	1.07	-106	-249	[-49, 557]	-0.77	1.49	38	241	404
	$\theta_b = 45^\circ$	[-856, -49]	1.87	2.12	2.71	-78	-204	[-20, 413]	-0.24	1.15	38	194	346
	$\tau_{\text{dust}}=1$	[-591, -37]	1.87	1.20	1.14	-83	-176	[-37, 332]	-0.50	1.45	32	138	265
	$\tau_{\text{dust}}=3$	[-580, -37]	1.95	1.25	1.31	-72	-169	[-37, 228]	-0.23	1.22	44	93	196
	ISM	[-568, 90]	3.12	1.88	1.19	-72	-99	[101, 378]	-0.19	1.15	113	237	242
	ISM+dust	[-603, 101]	3.06	2.12	1.40	44	-93	[182, 194]	-0.00	1.02	182	188	12
FeII* 2612	Fiducial							[-173, 183]	-0.34	1.24	-23	5	241
	$\phi = 0^\circ$							[-46, 183]	-0.16	1.22	11	67	172
	$\phi = 180^\circ$							[-190, 68]	-0.16	1.21	-46	-61	172
	$\theta_b = 80^\circ$							[-276, 241]	-0.46	1.29	-46	-17	316
	$\theta_b = 45^\circ$							[-18, 155]	-0.07	1.10	40	68	144
	$\tau_{\text{dust}}=1$							[-173, 114]	-0.23	1.21	-46	-28	207
	$\tau_{\text{dust}}=3$							[-150, 91]	-0.14	1.16	-46	-30	184
	ISM							[-184, 160]	-1.10	2.66	0	-9	138
	ISM+dust							[-138, 137]	-0.45	1.53	0	-1	161
FeII* 2626	Fiducial							[-171, 183]	-0.39	1.29	-46	5	217
	$\phi = 0^\circ$							[-52, 177]	-0.13	1.16	34	62	171
	$\phi = 180^\circ$							[-194, 63]	-0.13	1.16	-52	-66	143
	$\theta_b = 80^\circ$							[-280, 234]	-0.58	1.41	-52	-22	314
	$\theta_b = 45^\circ$							[6, 148]	-0.08	1.14	34	76	114
	$\tau_{\text{dust}}=1$							[-160, 126]	-0.25	1.23	-46	-17	194
	$\tau_{\text{dust}}=3$							[-171, 68]	-0.14	1.17	-46	-51	194
	ISM							[-194, 194]	-1.76	4.10	0	0	103
	ISM+dust							[-160, 114]	-0.47	1.70	0	-21	137
FeII* 2632	Fiducial							[-132, 119]	-0.16	1.12	16	-6	194
	$\phi = 0^\circ$							[-41, 130]	-0.08	1.09	45	44	142
	$\phi = 180^\circ$							[-155, 16]	-0.08	1.11	-41	-69	142
	$\theta_b = 80^\circ$							[-212, 159]	-0.23	1.14	16	-26	285
	$\theta_b = 45^\circ$							[-639, 102]	-0.18	1.14	-611	-271	684
	$\tau_{\text{dust}}=1$							[-121, 85]	-0.11	1.10	-52	-18	160
	$\tau_{\text{dust}}=3$							[-98, 16]	-0.05	1.08	-41	-41	103
	ISM							[-121, 130]	-0.55	1.81	5	4	137
	ISM+dust							[-121, 107]	-0.22	1.30	5	-6	148

NOTE. — Listed are the equivalent widths (intrinsic, absorption, and emission), the peak optical depth for the absorption $\tau_{\text{pk}} \equiv -\ln(I_{\text{min}})$, the velocity where the optical depth peaks v_τ , the optical depth-weighted velocity centroid of the emission line $v_{\bar{\tau}} \equiv \int dv v \ln[I(v)] / \int dv \ln[I(v)]$, the peak flux f_{pk} in emission, the velocity where the flux peaks v_f , the flux-weighted velocity centroid of the emission line $v_{\bar{f}}$ (occasionally affected by blends with neighboring emission lines), and the 90% width Δv_e . The v_{int}^a and v_{int}^e columns give the velocity range used to calculate the absorption and emission characteristics, respectively. These were defined by the velocities where the profile crossed 0.95 in the normalized flux.

profiles are compared against the fiducial model in Figure 13. Inspecting Mg II, one notes that the models with $1/3$ and $3n_{\text{H}}^{0,f}$ behave as expected. Higher/lower optical depths lead to greater/weaker Mg II $\lambda 2796$ absorption and stronger/weaker Mg II $\lambda 2803$ emission. In the extreme case of $n_{\text{H}}^0 = 10n_{\text{H}}^{0,f}$, the Mg II $\lambda 2803$ absorption and Mg II $\lambda 2796$ emission have nearly disappeared and one primarily observes very strong Mg II $\lambda 2796$ absorption and Mg II $\lambda 2803$ emission. In essence, this wind has converted all of the photons absorbed by the Mg II doublet into Mg II $\lambda 2803$ emission.

Similar behavior is observed for the Fe II transitions. Interestingly, the Fe II $\lambda 2586$ transitions never show significant emission, only stronger absorption with increasing n_{H}^0 . In fact, for $n_{\text{H}}^0 > 2n_{\text{H}}^{0,f}$ the peak optical depth of Fe II $\lambda 2586$ actually exceeds that for Fe II $\lambda 2600$ because the latter remains significantly filled-in by scattered photons. By the same token, the flux of the Fe II* $\lambda 2612$ emission increases with n_{H}^0 .

4.5. Summary Table

Table 4 presents a series of quantitative measures of the Mg II and Fe II absorption and emission lines for the fiducial model (§ 3) and a subset of the models presented in this section. Listed are the absorption and emission equivalent widths (W_{a} , W_{e}), the peak optical depth for the absorption τ_{pk} , the velocity where the optical depth peaks v_{τ} , the optical depth-weighted velocity centroid $v_{\bar{\tau}} \equiv \int dv v \ln[I(v)] / \int dv \ln[I(v)]$, the peak flux f_{pk} in emission, the velocity where the flux peaks v_f , and the flux-weighted velocity centroid of the emission line $v_{\bar{f}}$. We discuss several of these measures in § 6.

5. ALTERNATE WIND MODELS

This section presents several additional wind scenarios that differ significantly from the fiducial model explored in the previous sections. In each case, we maintain the simple assumption of isotropy.

5.1. The Lyman Break Galaxy Model

The Lyman break galaxies (LBGs), UV color-selected galaxies at $z \sim 3$, exhibit cool gas outflows in Si II, C II, etc. transitions with speeds up to 1000 km s^{-1} (e.g. Lowenthal et al. 1997; Pettini et al. 1998). Researchers have invoked these winds to explain enrichment of the intergalactic medium (e.g. Aguirre et al. 2001; Scannapieco et al. 2006), the origin of the damped Ly α systems (Nulsen et al. 1998; Schaye 2001), and the formation of ‘red and dead’ galaxies (e.g. Somerville et al. 2001). Although the presence of these outflows was established over a decade ago, the processes that drive them remain unidentified. Similarly, current estimates of the mass and energetics of the outflows suffer from orders of magnitude uncertainty.

Recently, Steidel et al. (2010, hereafter S10) introduced a model to explain jointly the average absorption they observed along the sightlines to several hundred LBGs and the average absorption in gas observed transverse to these galaxies. Their wind model is defined by two expressions: (i) a radial velocity law $v_{\text{r}}(r)$; and (ii) the covering fraction of optically thick ‘clouds’ $f_{\text{c}}(r)$. For the latter, S10 envision an ensemble of small, optically thick ($\tau \gg 1$) clouds that only partially cover the

galaxies. For the velocity law, they adopted the following functional form:

$$v_{\text{r}} = \left(\frac{A_{\text{LBG}}}{1 - \alpha} \right)^{1/2} [r_{\text{inner}}^{1-\alpha} - r^{1-\alpha}]^{1/2} \quad (5)$$

with A_{LBG} the constant that sets the terminal speed, r_{inner} the inner radius of the wind (taken to be 1 kpc), and α the power-law exponent that describes how steeply the velocity curve rises. Their analysis of the LBG absorption profiles implied a very steeply rising curve with $\alpha \approx 1.3$. This velocity expression is shown as a dotted line in Figure 14a.

The covering fraction of optically thick clouds, meanwhile, was assumed to have the functional form

$$f_{\text{c}}(r) = f_{\text{c,max}} \left(\frac{r}{r_{\text{inner}}} \right)^{-\gamma}, \quad (6)$$

with $\gamma \approx 0.5$ and $f_{\text{c,max}}$ the maximum covering fraction. From this expression and the velocity law, one can recover an absorption profile $I_{\text{LBG}}(v) = 1 - f_{\text{c}}[r(v)]$, written explicitly as

$$I_{\text{LBG}}(v) = 1 - f_{\text{c,max}} \left[r_{\text{inner}}^{1-\alpha} - \left(\frac{1-\alpha}{A_{\text{LBG}}} \right) v^2 \right]^{\gamma/(\alpha-1)}. \quad (7)$$

The resulting profile for $f_{\text{c,max}} = 0.6$, $\gamma = 0.5$, $\alpha = 1.3$, and $A_{\text{LBG}} = -192,000 \text{ km}^2 \text{ s}^{-2} \text{ kpc}^{-2}$ is displayed in Figure 14b.

In the following, we consider two methods for analyzing the LBG wind. Both approaches assume an isotropic wind and adopt the velocity law given by Equation 5. In the first model, we treat the cool gas as a diffuse medium with unit covering fraction and a radial density profile determined from the Sobolev approximation. We then apply the Monte Carlo methodology used for the other wind models to predict Mg II and Fe II line profiles. In the second LBG model, we modify our algorithms to more precisely mimic the concept of an ensemble of optically thick clouds with a partial covering fraction on galactic scales.

5.1.1. Sobolev Inversion

As demonstrated in Figure 14, the wind velocity for the LBG model rises very steeply with increasing radius before flattening at large radii. Under these conditions, the Sobolev approximation provides an accurate description of the optical depth for the flowing medium. The Sobolev line optical depth profile can be derived from the absorption profile (Equation 7),

$$\tau_{\text{LBG}}(v) = -\ln[I_{\text{LBG}}(v)] \quad (8)$$

This simple expression assumes that the source size is small compared the wind dimensions and neglects the effects of light scattered in the wind (for more general inversion formulae that do not make these assumptions, see Kasen et al. (2002)). The Sobolev approximation (Equation 1) provides a simple expression for the optical depth at each radius in terms of the local density and velocity gradient. In general, the velocity gradient must be taken along the direction of propagation of a photon, however

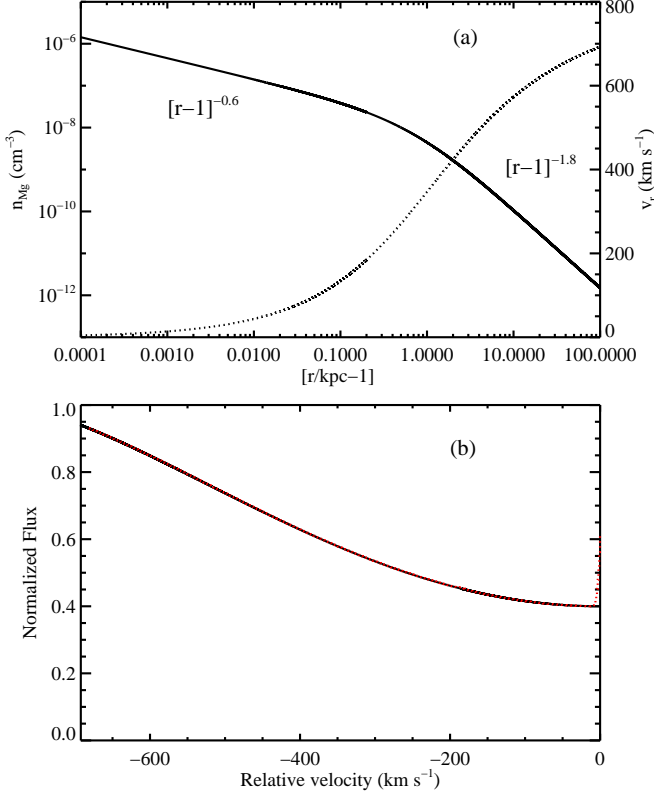


FIG. 14.— (a) The dotted curve shows the velocity law (labeled on the right axis) for the LBG model of S10 plotted against $(r/\text{kpc} - 1)$ to highlight the evolution in the quantities at small radii. For example, note how rapidly the velocity rises from $r = 1$ to 2 kpc. The solid curve shows the Sobolev solution for the Mg^+ gas density derived from the average absorption profile of LBG galaxies (see below). The density falls off initially as $(r/\text{kpc} - 1)^{-0.6}$ and then steepens to $(r/\text{kpc} - 1)^{-1.8}$. (b) The average profile for LBG cool gas absorption as measured and defined by S10 (black solid curve). Overplotted on this curve is a (red) dotted line that shows the $\text{Mg II } \lambda 2796$ absorption profile derived from the density (and velocity) law shown in the upper panel.

in this model the central source is relatively small and the radiation field is therefore primarily radially directed. In this case the velocity gradient in the radial direction, dv_r/dr , is the relevant quantity, and we may use Equation 1 to invert the optical depth and determine the density profile,

$$n_{\text{LBG}}(r) = \tau_{\text{LBG}}(r) \frac{|dv_r/dr|}{f_\ell \lambda_\ell^0} \left(\frac{m_e c}{\pi e^2} \right). \quad (9)$$

The solid curve in Figure 14a shows the resultant density profile for Mg^+ assuming that the $\text{Mg II } \lambda 2796$ line follows the intensity profile drawn in Figure 14b. This is a relatively extreme density profile. From the inner radius of 1 kpc to 2 kpc, the density drops by over 2 orders of magnitude including nearly one order of magnitude over the first 10 pc. Beyond 2 kpc, the density drops even more rapidly, falling orders of magnitude from 2 to 100 kpc.

We verified that the Sobolev-derived density profile shown in Figure 14a reproduces the proper absorption profile by discretizing the wind into a series of layers and calculating the integrated absorption profile. This calculation is shown as a dotted red curve in Figure 14b; it is an excellent match to the desired profile (black curve).

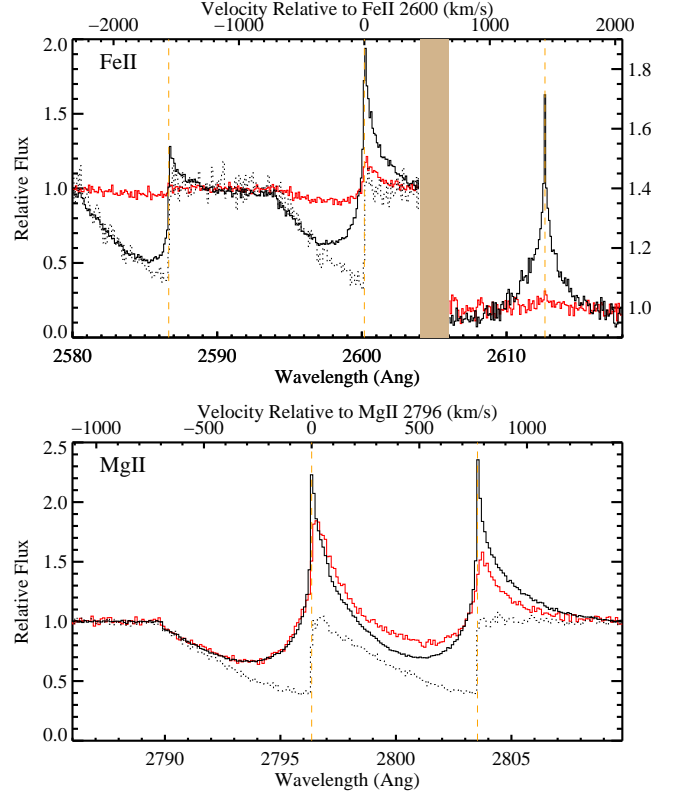


FIG. 15.— Profiles of the Fe II and Mg II profiles for the two LBG models considered: (red) the profiles predicted using the Sobolev approximation and (black) a model constructed to faithfully represent the wind model advocated by S10. The dotted line shows the absorption profiles of the latter model if one were to neglect scattered and re-emitted photons. Similar to the fiducial model (Figure 4), scattered and re-emitted photons significantly modify the absorption profiles (especially Mg II and Fe II $\lambda 2600$) and produce strong emission lines. The result, for Mg II especially, is a set of profiles that do not match the average observed LBG absorption profile.

To calculate the optical depth profiles for the other Mg II and Fe II transitions, we assume $n_{\text{Fe}^+} = n_{\text{Mg}^+}/2$ and also scale τ by the $f\lambda$ product.

We generated Mg II and Fe II profiles for this LBG-Sobolev wind using the 1D algorithm with no dust extinction; these are shown as red curves in Figure 15. For this analysis, one should focus on the Mg II $\lambda 2796$ transition. The dotted line in the Figure shows the intensity profile when one ignores re-emission of absorbed photons. By construction, it is the same profile⁹ described by Equation 7 and plotted in Figure 14b. In comparison, the full model (solid, red curve) shows much weaker absorption, especially at $v = 0$ to -300 km s^{-1} because scattered photons fill in the absorption profile. In this respect, our LBG-Sobolev model is an inaccurate description of the observations which show more uniform equivalent widths among differing transitions (S10). The model also predicts significant emission in the Mg II lines and several of the Fe II* transitions. Emission associated with cool gas has been observed for Si II* transitions in LBGs (Pettini et al. 2002; Shapley et al. 2003), but the Fe II* transitions modeled here lie in the near-

⁹ The other transitions in the LBG-Sobolev model are significantly weaker than the input model because these are scaled down by $f\lambda$ and for Fe II the reduced Fe^+ abundance.

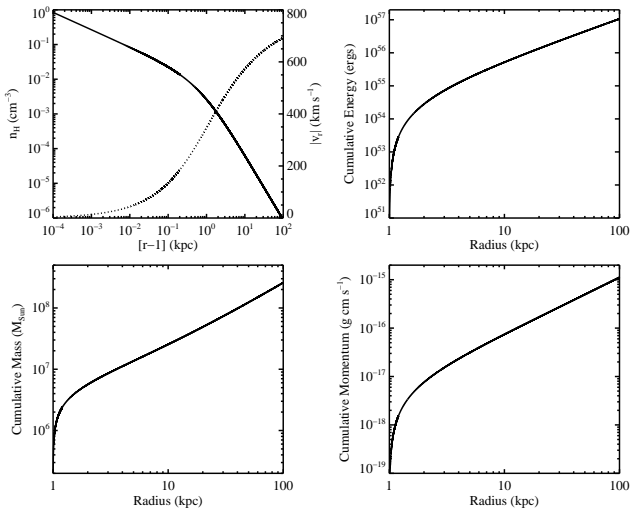


FIG. 16.— The upper left panel shows the density (solid) and velocity (dotted) laws for the LBG-Sobolev wind model (Figure 14). The remaining panels show the cumulative mass, energy, and momentum of this flow. All of the curves rise very steeply at small radii and then rise steadily to large radii. The principal result is that the majority of mass, energy, and momentum in the wind are contained at large radii. We derive similar results for the LBG-partial covering model if we assume the wind is composed of identical clouds optically thick to strong metal-line transitions (e.g. Si II 1526). The energy and momentum in the outer regions of the outflow may be very difficult to generate with standard galactic-scale wind scenarios.

IR and have not yet been investigated. On the other hand, there have been no reported detections of significant line-emission related to low-ion resonance transitions (e.g. Mg II) in LBGs, only $z \leq 1$ star-forming galaxies (Weiner et al. 2009; Rubin et al. 2010b). The principal result of the LBG-Sobolev model is that the scattering and re-emission of absorbed photons significantly alters the predicted absorption profiles for the input model. This is, of course, an unavoidable consequence of an isotropic, dust-free model with unit covering fraction.

Because we have explicit velocity and density profiles for the LBG-Sobolev model, it is straightforward to calculate the radial distributions of mass, energy, and momentum of this wind. These are shown in cumulative form in Figure 16. Before discussing the results, we offer two cautionary comments: (i) the conversion of n_{Mg^+} to n_{H} assumes a very poorly constrained scalar factor of $10^{5.47}$. One should give minimal weight to the absolute values for any of the quantities; (ii) the Sobolev approximation is not a proper description of the S10 LBG wind model (see the following sub-section). These issues aside, we may inspect Figure 16 to reveal global properties of this LBG-Sobolev wind. One obvious result is that all of the curves rise very steeply at small radii. We find, for example, that $\approx 10\%$ of the mass is contained within the inner 2 kpc. All of the curves continue to rise, however, such that the majority of energy, mass, and momentum in the wind is transported by its outermost layers (i.e., $r > 20$ kpc). This is somewhat surprising given that the density is ≈ 5 orders of magnitude lower at these radii than at $r = 1$ pc. More importantly, we question whether any physical process could produce a wind with such extreme profiles.

5.1.2. Partial Covering Fraction

In the previous sub-section, we described a Sobolev inversion that reproduces the average absorption profile of LBGs in cool gas transitions when scattered photons are ignored. A proper analysis that includes scattered photons, however, predicts line-profiles that are qualitatively different from the observations because scattered photons fill-in absorption and generate significant line-emission (similar to the fiducial wind model; § 3). We also argued that the implied mass, energy, and momentum distributions of this wind (Figure 16) were too extreme. This LBG-Sobolev model, however, is not precisely the one introduced by S10; those authors proposed an ensemble of optically thick clouds with a partial covering fraction described by Equation 6. In contrast, the LBG-Sobolev model assumes a diffuse medium with a declining density profile but a unit covering fraction. One may question, therefore, whether these differences lead to the failures of the LBG-Sobolev model.

To more properly model the LBG wind described in S10, we performed the following Monte Carlo calculation. First, we propagate a photon from the source until its velocity relative to line-center resonates with the wind (the photon escapes if this never occurs). The photon then has a probability $P = f_c(r)$ of scattering. If it scatters, we track the photon until it comes into resonance again¹⁰ or escapes the system. In this model, all of the resonance transitions are assumed to have identical (infinite) optical depth at line center.

The results of the full calculation (absorption plus scattering) are shown as the black curve in Figure 15. Remarkably, the results are essentially identical to the LBG-Sobolev calculation for the Mg II $\lambda 2796$ transition; scattered photons fill-in the absorption profiles at $v \approx 0 \text{ km s}^{-1}$ and yield significant emission lines at $v \gtrsim 0 \text{ km s}^{-1}$. Similar results are observed for the other resonance lines and significant emission is observed for the Fe II* transitions, centered at $\delta v \approx 0 \text{ km s}^{-1}$. In contrast to the Mg II profiles, the Fe II $\lambda 2586$ line much more closely resembles its intrinsic profile (dotted curves). This occurs because most of these absorbed photons fluoresce into Fe II* emission. The equivalent width of Fe II $\lambda 2586$ even exceeds that for Fe II $\lambda 2600$, an inversion that, if observed, would strongly support this model.

A robust conclusion of our analysis is that these simple models cannot reproduce the observed profiles of resonantly trapped lines (like the Mg II doublet) because of the emission from scattered photons. In particular, the observations show much greater opacity at velocities within $\approx 100 \text{ km s}^{-1}$ of systemic (S10). In order to achieve a significant opacity at $\delta v \approx 0 \text{ km s}^{-1}$, one must either suppress the line-emission (e.g. with severe dust extinction or anisotropic winds) or include a substantial ISM component that absorbs light at $\delta v \gtrsim 0 \text{ km s}^{-1}$ (e.g. § 4.3). Absent such corrections (which may be insufficient), we conclude that the LBG model introduced by S10 is not a valid description of the data. Also, similar to our LBG-Sobolev calculation (Figure 14), this clump

¹⁰ Because this wind has a monotonically increasing velocity law, the photon may only scatter again if a longer wavelength transition is available, e.g. Mg II $\lambda 2803$ for a scattered Mg II $\lambda 2796$ photon.

model predicts the majority of mass, energy, and momentum are carried in the outer regions of the wind. In fact, for clumps that are optically thick to strong metal-line transitions (e.g. Si II 1526) we estimate¹¹ that the wind would carry nearly a total mass of $\approx 10^{10} M_\odot$, with the majority at large radii.

The resonant line-emission predicted for Mg II should also arise in other transitions. Indeed, we caution that the C IV line-emission observed in LBG spectra (e.g. Pettini et al. 2002) may result from the galactic-scale outflow, not only the stellar winds of massive stars. A proper treatment of these radiative transfer effects is required to quantitatively analyze these features.

5.2. Radiation Pressure

As discussed in the Introduction, the importance of various physical mechanisms in driving galactic outflows remains an open question. Several studies advocate a primarily energy-driven wind scenario, in which the hot wind produced by the thermalized energy from SNe ejecta entrains cool clouds via ram pressure (e.g. Chevalier & Clegg 1985; Heckman et al. 1990; Strickland & Heckman 2009). Alternatively, momentum deposition by photons emitted by luminous star clusters onto dust grains in the ISM may also play an integral role in driving large-scale outflows (e.g. Murray et al. 2005, 2010). Both of these mechanisms likely contribute more or less significantly in a given galaxy; however, the latter (radiation-pressure driving) has the added advantage that it does not destroy cool gas clouds as it acts. Here we explore the line-profiles produced by a radiation-pressure driven wind model as described by Murray et al. (2005).

These authors start by assuming the galaxy has luminosity L and is an isothermal sphere with mass profile $M_{gal}(r) = 2\sigma^2 r/G$, where σ is the velocity dispersion. The gas mass profile is simply $M_g(r) = f_g M_{gal}(r)$, with f_g a constant gas fraction. The dust has opacity κ and is optically thin, such that the force per unit mass of wind material due to radiation is $\frac{\kappa L}{4\pi cr^2}$. Ignoring gas pressure, and assuming a steady state for the flow (i.e., the mass outflow rate, dM_{wind}/dt , is constant), the momentum equation for the wind is

$$v_r \frac{dv_r}{dr} = -\frac{GM_{gal}(r)}{r^2} + \frac{\kappa L}{4\pi cr^2}. \quad (10)$$

Substituting $2\sigma^2 r/G$ for $M_{gal}(r)$ and solving for v_r , Murray et al. (2005) find

$$v_r(r) = 2\sigma \sqrt{R_g \left(\frac{1}{R_0} - \frac{1}{r} \right) + \ln(R_0/r)} \quad (11)$$

(their Equ. 26), where $v_r = 0$ at R_0 and $R_g = \frac{\kappa L}{8\pi c\sigma^2}$. The corresponding density profile for the gas is given by

$$n_H(r) = \frac{dM_{wind}/dt}{m_p r^2 v(r)}, \quad (12)$$

with m_p the mass of the hydrogen atom. Similar to the fiducial wind model, this wind has a decreasing density

¹¹ Note that this estimate differs from the LBG-Sobolev calculation shown in Figure 16 because the latter assumes a diffuse medium with unit filling factor.

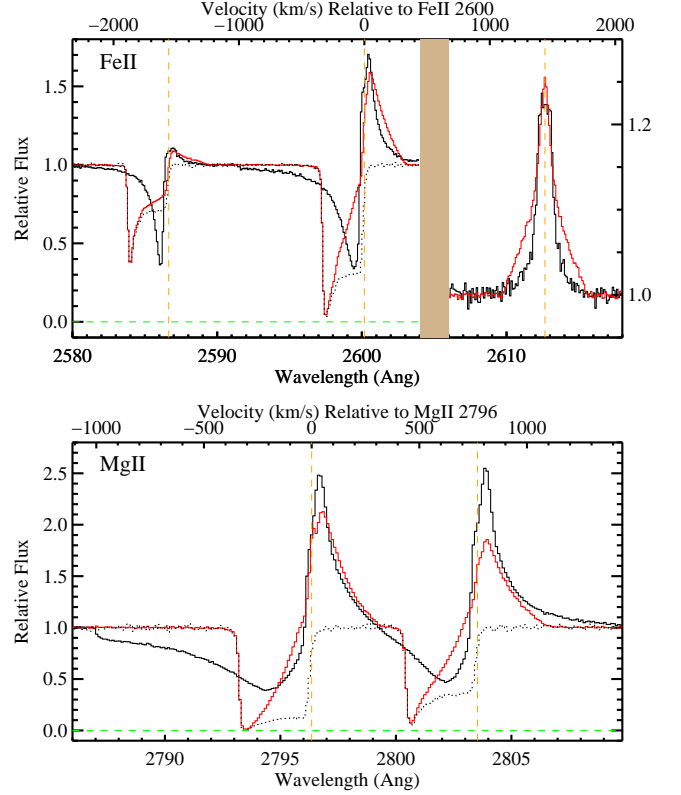


FIG. 17.— Mg II and Fe II profiles for a radiation-driven wind model (red) compared against the fiducial wind model (black). In contrast to the fiducial model, the optical depth peaks at large velocity (here $\delta v \approx -350 \text{ km s}^{-1}$). At these velocities, the absorption is not filled-in by scattered photons and one recovers absorption lines that closely resemble the intrinsic optical depth profile (dotted curve). Although the Mg II absorption profiles are very different from the fiducial model, the Mg II line-emission has similar peak flux and velocity centroids. The Fe II* emission also has a similar equivalent width, yet the lines are much broader in the radiation-driven model.

law with n_H roughly proportional to r^{-2} . In contrast to the fiducial model, the velocity law is nearly constant with radius before decreasing sharply at large radii. To produce a wind whose Mg II $\lambda 2796$ optical depth profile peaks at $\tau_{2796}^{\max} \gtrsim 10$, we set $R_0 = r_{\text{inner}} = 1 \text{ kpc}$, $R_g = 4 \text{ kpc}$, and $\sigma = 125 \text{ km s}^{-1}$. The density peaks at $r = r_{\text{inner}}$ where $n_H^0 = 0.03 \text{ cm}^{-3}$. The velocity, meanwhile, peaks at $r = R_g$ with $v_r \approx 400 \text{ km s}^{-1}$. This corresponds to a mass flow of $dM_{wind}/dt \approx 0.2 M_\odot \text{ yr}^{-1}$.

Figure 17 presents the Mg II and Fe II profiles for this radiation-driven wind model compared against the fiducial wind model. In contrast to the fiducial model, the optical depth peaks at much larger velocity (here $\delta v \approx -400 \text{ km s}^{-1}$). At these velocities, the absorption is not filled-in by scattered photons and one recovers absorption lines that more closely follow the intrinsic optical depth profile (dotted curve). The Mg II line-emission, meanwhile, has similar peak flux and velocity centroids to the fiducial model (see also Table 6). The Fe II* emission also has a similar equivalent width, yet the lines of the radiation-driven model are much broader. This reflects the fact that the majority of absorption occurs at $\delta v \ll 0 \text{ km s}^{-1}$. The kinematics of Fe II* line-emission, therefore, independently diagnose the intrinsic optical depth profile of the flow. We conclude that the

TABLE 5
WIND PARAMETERS: POWER-LAW MODELS

Label	$n(r)$	n_{H}^0	$v(r)$	v^0	$\log \tau_{2796}^{\text{max}}$
A	r^{-3}	0.4000	$r^{-2.0}$	2.0	0.8
B	r^{-3}	0.5000	$r^{-1.0}$	50.0	1.1
C	r^{-3}	0.3000	$r^{0.5}$	100.0	1.8
D	r^0	0.0100	$r^{-2.0}$	2.0	2.1
E	r^0	0.0100	$r^{-1.0}$	50.0	1.7
F	r^0	0.0200	$r^{0.5}$	100.0	1.6
G	r^2	0.0100	$r^{-2.0}$	2.0	4.4
H	r^2	0.0010	$r^{-1.0}$	50.0	3.2
I	r^2	0.0001	$r^{0.5}$	100.0	1.8

NOTE. — For velocity laws that decrease with radius, the normalization v^0 refers to the velocity at $r = r_{\text{outer}}$ instead of $r = r_{\text{inner}}$. All models assume a Doppler parameter $b = 15 \text{ km s}^{-1}$, full isotropy, and a dust-free environment.

radiation-driven model has characteristics that are qualitatively similar to the fiducial model (e.g. strong blue-shifted absorption and significant line-emission) with a few quantitative differences that, in principle, could distinguish them with high fidelity observations.

5.3. Power-Law Models

The fiducial model assumed power-law descriptions for both the density and velocity laws (Equations 3,4). The power-law exponents were arbitrarily chosen, i.e. with little physical motivation. In this sub-section, we cursorily explore the results for a series of other power-law expressions, also arbitrarily defined. Our intention is to illustrate the diversity of Mg II and Fe II profiles that may result from modifications to the density and velocity laws. We consider three different density laws ($n_{\text{H}} \propto r^{-3}, r^0, r^2$) and three different velocity laws ($v_{\text{r}} \propto r^{-2}, r^{-1}, r^{0.5}$) for nine wind models (Table 5, Figure 18a). Each of these winds extends over the same inner and outer radii as the fiducial model. The density and velocity normalizations n_{H}^0, v^0 have been modified to yield a Mg II $\lambda 2796$ optical depth profile that peaks at $\tau_{2796}^{\text{max}} \approx 10 - 10^3$ and then usually decreases to $\tau_{2796} < 1$ (Figure 18b). This choice of normalization was observationally driven to yield significant absorption lines. All models assume a Doppler parameter $b = 15 \text{ km s}^{-1}$, full isotropy, and a dust-free environment. Lastly, the abundances of Mg^+ and Fe^+ scale with hydrogen as in the fiducial model (Table 2).

Figure 19 presents the Mg II and Fe II profiles for the full suite of power-law models (see also Table 6). Although these models differ qualitatively from the fiducial model in their density and velocity laws, the resultant profiles share many of the same characteristics. Each shows significant absorption at $\delta v < 0 \text{ km s}^{-1}$, extending to the velocity where τ_{2796} drops below 0.1 (Figure 18b). All of the models also exhibit strong line-emission, primarily at velocities $\delta v \sim 0 \text{ km s}^{-1}$. This emission fills-in the Mg II absorption at $\delta v \gtrsim -100 \text{ km s}^{-1}$ such that the profiles rarely achieve a relative flux less than ≈ 0.1 at these velocities. Similar to the radiation-driven wind (§ 5.2), the power-law models that have significant opacity at $\delta v < -300 \text{ km s}^{-1}$ tend to have larger peak optical depths. Another commonality is the weak or absent line-emission at Fe II $\lambda 2586$; one instead notes strong

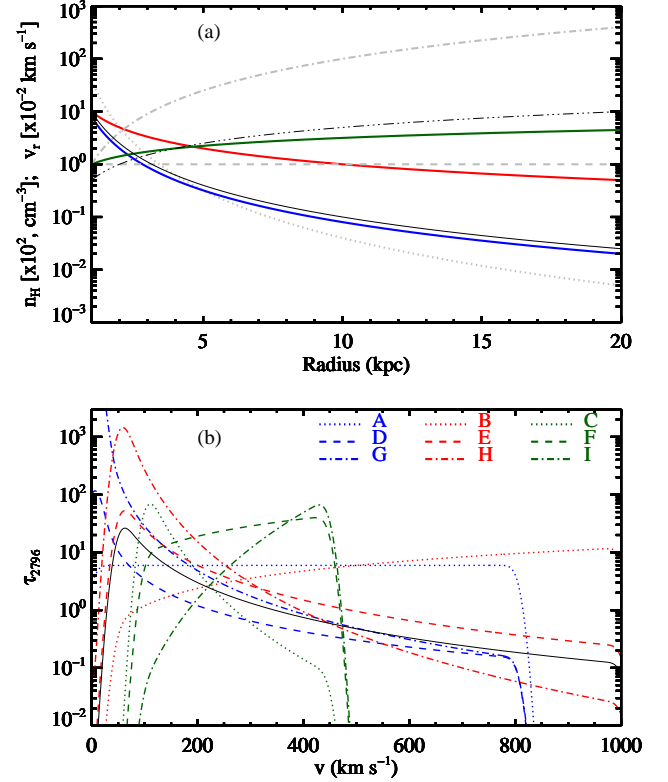


FIG. 18.— In panel (a) we illustrate the density (gray curves; dashed — $n_{\text{H}}^0 \propto r^0$, dotted — $n_{\text{H}}^0 \propto r^{-3}$, dot-dash — $n_{\text{H}}^0 \propto r^2$) and velocity laws (colored; green — $v \propto r^{0.5}$, red — $v \propto r^{-1}$, blue — $v \propto r^{-2}$) for a series of power-law models (Table 5). For comparison we also plot the velocity and density laws for the fiducial model (thin, black curves). Panel (b) plots the optical depth profiles of the Mg II $\lambda 2796$ line for the nine models built from the density and velocity laws of panel (a). Each of these were normalized to have peak optical depths of 10 to 1000 and to be optically thin at small or large velocity.

Fe II* $\lambda 2612$ emission that generally exceeds the equivalent width of the fiducial model. One also notes that the width of the Fe II* emission is systematically higher for models where the optical depth in absorption peaks at large velocity from the systemic. One of the few obvious distinctions between these models and the fiducial wind is the higher peak optical depth of absorption in the Fe II $\lambda 2600$ transition. This occurs primarily because these models have higher intrinsic optical depths (i.e. higher n_{Fe^+} values).

While there is commonality between models, the specific characteristics of the absorption/emission profiles do exhibit significant diversity. Table 6 compares measures of the absorption and emission profiles against the fiducial model. In detail, the line profiles differ in their peak optical depths, the velocity centroids of absorption/emission, and their equivalent widths. We find that many of the differences are driven by differences in the velocity laws, i.e. the kinematics of the outflow. At the same time, models with very different density/velocity laws can produce rather similar results. For example, profiles that have declining opacity with increasing velocity offset from systemic can be obtained with a radial velocity law that increases (e.g. the fiducial model) or decreases (model D). The implication is that absorption

TABLE 6
LINE DIAGNOSTICS FOR THE FIDUCIAL MODEL AND VARIANTS

Transition	Model	v_{int}^a (km s ⁻¹)	W_i (Å)	W_a (Å)	τ_{pk}	v_τ (km/s)	$v_{\bar{\tau}}$ (km/s)	v_{int}^e (km/s)	W_e (Å)	f_{pk}	v_f (km/s)	$v_{\bar{f}}$ (km/s)	Δv_e (km/s)
MgII 2796	Fiducial	[-1009, -43]	4.78	2.83	0.94	-215	-372	[-32, 311]	-1.77	2.48	32	117	215
	LBG Sob.	[-687, -86]	2.62	1.35	0.45	-247	-347	[-65, 257]	-1.02	1.84	21	90	193
	LBG Cov.	[-698, -65]	2.67	1.40	0.41	-258	-344	[-54, 214]	-0.93	2.23	0	72	172
	Radiation	[-365, -65]	2.86	1.72	3.00	-301	-250	[-54, 322]	-1.74	2.13	53	119	236
	A	[-848, -22]	9.29	5.02	2.92	-773	-499	[-22, 171]	-1.34	3.30	21	64	118
	B	[-1084, -65]	11.08	7.54	3.00	-976	-589	[-65, 193]	-1.83	2.89	0	50	172
	C	[-451, -65]	2.54	1.82	1.86	-204	-200	[-65, 332]	-1.79	2.09	0	116	247
	D	[-794, 21]	4.21	2.14	1.11	-11	-276	[32, 311]	-1.57	3.58	43	141	172
MgII 2803	Fiducial	[-437, -41]	3.29	1.19	0.76	-148	-193	[-41, 676]	-2.24	2.55	34	269	449
	LBG Sob.	[-426, -73]	1.53	0.46	0.24	-244	-244	[-62, 387]	-0.80	1.58	23	154	332
	LBG Cov.	[-533, -73]	2.56	0.98	0.37	-233	-285	[-51, 558]	-1.48	2.35	2	227	396
	Radiation	[-362, -84]	2.32	1.29	2.65	-308	-256	[-73, 323]	-1.31	1.86	45	115	246
	A	[-554, -41]	7.06	1.98	0.78	-330	-293	[-41, 805]	-5.72	5.03	13	304	610
	B	[-554, -169]	5.74	1.80	1.27	-372	-359	[-84, 1008]	-7.34	4.20	2	338	749
	C	[-405, -73]	2.17	1.49	1.85	-169	-179	[-73, 355]	-1.52	1.94	77	122	246
	D	[-30, 13]	3.69	0.19	0.77	-9	-1	[23, 558]	-1.48	3.33	34	251	332
FeII 2586	Fiducial	[-348, -35]	0.82	0.61	1.01	-70	-119	[-35, 128]	-0.10	1.11	35	47	128
	LBG Sob.	[-151, -46]	0.18	0.04	0.07	-139	-99	[-12, 35]	-0.01	1.05	0	12	35
	LBG Cov.	[-684, -12]	2.38	1.93	0.65	-162	-276	[-12, 360]	-0.34	1.33	12	170	313
	Radiation	[0, 0]	1.00	0.00	0.02	0	0	[12, 255]	-0.11	1.09	35	132	220
	A	[-812, -12]	1.88	1.66	0.33	-742	-422	[-12, 232]	-0.12	1.12	23	109	197
	B	[-1009, -186]	2.20	1.97	0.60	-951	-694	[-93, 418]	-0.24	1.09	12	161	429
	C	[-278, -81]	0.79	0.71	2.51	-116	-132	[-70, 162]	-0.10	1.08	93	46	174
	D	[-209, 23]	0.88	0.68	3.00	-12	-26	[35, 70]	-0.01	1.03	46	52	35
FeII 2600	Fiducial	[-580, -37]	1.87	1.18	1.08	-83	-181	[-37, 459]	-0.83	1.70	32	191	312
	LBG Sob.	[-453, -72]	0.55	0.24	0.11	-187	-263	[-26, 228]	-0.21	1.23	20	99	208
	LBG Cov.	[-695, -60]	2.43	1.38	0.44	-360	-336	[-49, 493]	-1.12	2.02	9	203	381
	Radiation	[-360, -26]	2.21	1.44	3.00	-303	-247	[-26, 320]	-0.84	1.59	44	138	242
	A	[-822, -26]	4.61	3.51	1.05	-753	-455	[-26, 793]	-1.78	2.34	9	347	612
	B	[-1018, -199]	5.10	4.20	1.88	-960	-701	[-176, 1001]	-2.84	1.86	-3	371	935
	C	[-360, -72]	1.34	1.09	2.04	-141	-154	[-72, 228]	-0.62	1.43	78	75	219
	D	[-430, 20]	1.68	1.13	3.00	-14	-58	[32, 309]	-0.31	1.47	44	163	219
FeII* 2612	Fiducial							[-173, 183]	-0.34	1.24	-23	5	241
	LBG Sob.							[-69, 57]	-0.04	1.07	0	-6	115
	LBG Cov.							[-356, 436]	-1.04	1.79	0	35	563
	Radiation							[-299, 298]	-0.50	1.26	0	-1	425
	A							[-402, 574]	-0.88	1.35	0	80	735
	B							[-402, 597]	-0.88	1.14	34	94	873
	C							[-184, 172]	-0.40	1.20	-81	-6	241
	D							[-115, 114]	-0.47	2.37	0	-1	103
FeII* 2626	Fiducial							[-171, 183]	-0.39	1.29	-46	5	217
	LBG Sob.							[-23, 46]	-0.03	1.06	23	11	57
	LBG Cov.							[-251, 274]	-0.28	1.22	0	11	434
	Radiation							[-286, 263]	-0.60	1.42	0	-11	343
	A							[-663, 320]	-1.60	1.71	0	-152	720
	B							[-891, 320]	-1.45	1.22	0	-270	1039
	C							[-171, 160]	-0.46	1.24	57	-5	217
	D							[-160, 148]	-0.87	3.53	0	-5	103
FeII* 2632	Fiducial							[-132, 119]	-0.16	1.12	16	-6	194
	LBG Sob.							[-29, 16]	-0.01	1.07	-7	-7	46
	LBG Cov.							[-292, 301]	-0.53	1.36	5	4	479
	Radiation							[-235, 210]	-0.23	1.12	5	-12	353
	A							[-326, 370]	-0.59	1.19	-7	15	581
	B							[-326, 563]	-0.78	1.17	-314	108	741
	C							[-143, 153]	-0.19	1.10	62	5	228
	D							[-86, 96]	-0.23	1.63	5	4	91

NOTE. — Listed are the equivalent widths (intrinsic, absorption, and emission), the peak optical depth for the absorption $\tau_{\text{pk}} \equiv -\ln(I_{\text{min}})$, the velocity where the optical depth peaks v_τ , the optical depth-weighted velocity centroid $v_{\bar{\tau}} \equiv \int dv v \ln[I(v)] / \int dv \ln[I(v)]$, the peak flux f_{pk} in emission, the velocity where the flux peaks v_f , the flux-weighted velocity centroid of the emission line $v_{\bar{f}}$ (occasionally affected by blends with neighboring emission lines), and the 90% width Δv_e . The v_{int}^a and v_{int}^e columns give the velocity range used to calculate the absorption and emission characteristics, respectively. These were defined by the velocities where the profile crossed 0.95 in the normalized flux. [See the electronic version for the complete Table].

profiles alone are likely insufficient to fully characterize the physical characteristics of the outflow.

6. DISCUSSION

We now discuss the principal results of our analysis and comment on the observational consequences and implications.

The previous sections presented idealized wind models for cool gas outflows, and explored the absorption/emission profiles of the Mg II $\lambda\lambda 2796, 2803$ doublet and the Fe II UV1 multiplet. In addition to the ubiquitous presence of blue-shifted absorption, the wind models also predict strong line-emission in both resonance and non-resonance transitions. For isotropic and dust-free scenarios, this is due to the simple conservation of photons: every photon emitted by the source eventually escapes the system to maintain zero total equivalent width. A principal result of this paper, therefore, is that galaxies with observed cool gas outflows should also generate detectable line-emission.

Indeed, line-emission from low-ion transitions has been reported from star-forming galaxies that exhibit cool gas outflows. This includes emission related to Na I (Phillips 1993; Chen et al. 2010), Mg II emission (Weiner et al. 2009; Rubin et al. 2010b), Si II* emission from LBGs (Shapley et al. 2003), and, most recently, significant Fe II* emission (Rubin et al. 2010a). A variety of origins have been proposed for this line-emission including AGN activity, recombination in H II regions, and back-scattering off the galactic-scale wind. Our results suggest that the majority of the observed line-emission is from scattered photons in the cool gas outflows of these star-forming galaxies. Indeed, line-emission should be generated by all galaxies driving a cool gas outflow.

On the other hand, there are many examples of galaxies where blue-shifted absorption is detected yet the authors report no significant line emission. This includes Na I flows (Rupke et al. 2005a; Martin 2005; Sato et al. 2009), Mg II and Fe II absorption in ULIRGS (Martin & Bouché 2009), and the extreme Mg II outflows identified by Tremonti et al. (2007). Similarly, there have been no reports of resonance line-emission from low-ion transitions in the LBGs¹², and many $z \lesssim 1$ galaxies show no detectable Mg II or Fe II* emission despite significant blue-shifted absorption (Rubin et al., in prep). These non-detections appear to contradict a primary conclusion of this paper. We are motivated, therefore, to reassess several of the effects that can reduce the line-emission and consider whether these prevent its detection in many star-forming galaxies.

Dust is frequently invoked to explain the suppression of line-emission for resonantly trapped transitions (e.g. Ly α). Indeed, a photon that is trapped for many scatterings within a dusty medium will be preferentially extinguished relative to a non-resonant photon. In § 4.2, we examined the effects of dust extinction on Mg II and Fe II emission. The general result (Figure 11) is a modest reduction in flux that scales as $(1+\tau_{\text{dust}})^{-1}$ instead of $\exp(-\tau_{\text{dust}})$. Although the Mg II photons are reso-

nantly trapped, they require only one to a few scatterings to escape the wind thereby limiting the effects of dust. This reflects the moderate opacity of the Mg II doublet (e.g. relative to Ly α) and also the velocity law of the fiducial wind model. In scenarios where the Mg II photons are more effectively trapped, dust does suppress the emission (e.g. in the ISM+wind model from § 4.3). In contrast to Mg II, the Fe II resonance photons may be converted to non-resonant photons that freely escape the wind. Therefore, a wind model that traps Mg II photons for many scatterings does not similarly trap Fe II $\lambda\lambda 2586, 2600$ photons. The effects of dust are much reduced and, by inference, the same holds for any other set of transitions that are coupled to a fine-structure level (e.g. Si II/Si II*). In summary, dust does reduce the line flux relative to the continuum, but it generally has only a modest effect on the predicted Mg II emission and a minor effect on Fe II* emission.

Another factor that may reduce line-emission is wind anisotropy. The flux is lower, for example, if one eliminates the backside to the wind (e.g. the source itself could shadow a significant fraction of the backside). Similarly, a bi-conical wind can have significantly lower line-emission, at least for the fiducial model (§ 4.1). For the anisotropic winds explored in this paper, the line-emission scales roughly as $\Omega/4\pi$ where Ω is the angular extent of the wind¹³. Because we require that the wind points toward us, it is difficult to reduce Ω much below 2π and, therefore, anisotropy reduces the emission by a factor of order unity. Similarly, an anisotropically emitting source would modify the predicted line-emission. For example, if the backside of the galaxy were brighter/fainter then would one predict brighter/fainter emission relative to the observed continuum. To reduce the emission, the brightest regions of the galaxy would need to be oriented toward Earth. Although this would not be a generic orientation, most spectroscopic samples are magnitude-limited and biased towards detecting galaxies when observed at their brightest. In principle, this might imply a further reduction of order unity.

Together, dust and anisotropic models may reduce the line-emission of Mg II and Fe II by one to a few factors of order unity. For some galaxies, these effects may explain the absence of significant line-emission, but they may not be sufficient to preclude its detection.

There is another (more subtle) effect that could greatly reduce the observed line-emission: slit-loss. As described in Figure 6, emission from the wind is spatially extended with a non-zero surface brightness predicted at large radii. This implies a non-negligible luminosity emitted beyond the angular extent of the galaxy. The majority of observations of star-forming galaxies to date have been taken through a spectroscopic slit designed to cover the brightest continuum regions. Slits with angular extents of $1 - 1.5''$ subtend roughly $8 - 15$ kpc for galaxies at $z > 0.5$. Therefore, a $1''$ slit covering a galaxy with our fiducial wind would cover less than half the wind. The result is reduced line-emission when compared to the galaxy continuum.

We explore the effects of slit-loss as follows. We model

¹² Pettini et al. (2000) reported and analyzed C IV line-emission from the lensed LBG cb58, attributing this flux to stellar winds. We caution, however, that the galactic-scale wind proposed for cb58 should also have contributed to the C IV line-emission.

¹³ There is also a first order dependence on the actual orientation of the wind, with maximal emission when the backside is fully viewed.

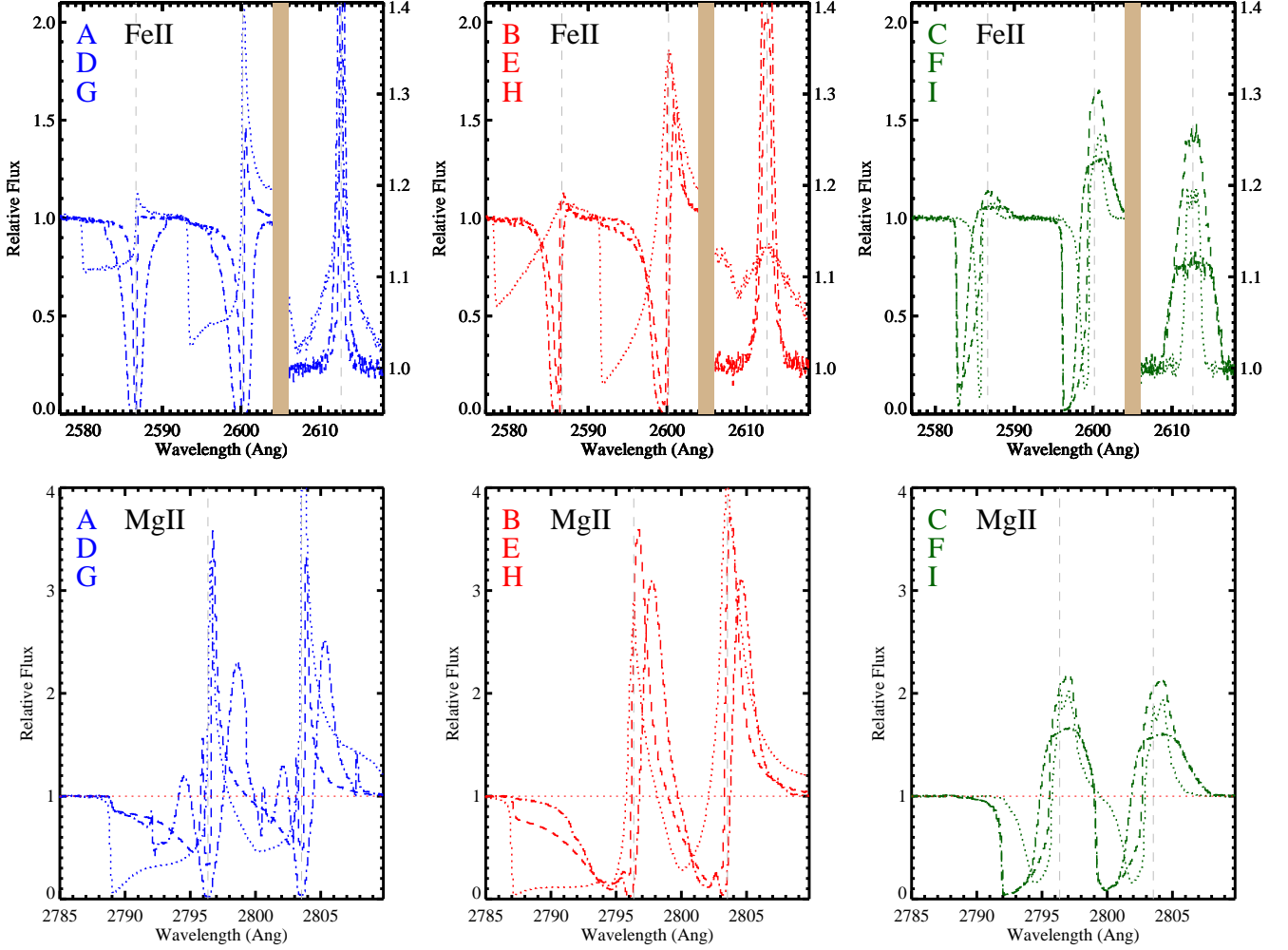


FIG. 19.— Mg II and Fe II profiles for a series of power-law wind models (see Table 5 for details). These panels reveal the diversity of absorption and emission that results from a set of intrinsic optical depth profiles that have relatively modest differences (Figure 18b). As designed, all of the models show significant absorption blueward of systemic velocity. As important, each shows strong line-emission at $\delta v \sim 0 \text{ km s}^{-1}$, with the flux proportional to the degree of absorption. We also note that the width of the Fe II* $\lambda 2612$ emission scales with the velocity offset of peak optical depth for the Fe II $\lambda 2586$ absorption. Therefore, the emission kinematics trace the intrinsic optical depth profile.

the slit as a perfect, infinitely-long rectangle centered on the galaxy. We then tabulate the equivalent width of the line-emission through slits with a range of widths, parameterized by $r_{\tau_S=0.2}$: twice the radius where the wind has a Sobolev optical depth of $\tau_S = 0.2$. The line-emission will be weak beyond this radius because the photons have only a low probability of being scattered. For the fiducial wind model, the Mg II $\lambda 2796$ transition has $r_{\tau_S=0.2} \approx 15 \text{ kpc}$ (Figure 3). The predicted equivalent width in emission W_e relative to the absorption equivalent width W_a is presented in Figure 20 for a series of transitions for the fiducial wind model (black curves). The W_e/W_a curves rise very steeply with increasing slit width and then plateau when the slit width reaches $\approx r_{\tau_S=0.2}$. For the fiducial model, the emission is concentrated toward the source; this derives from the density and velocity profiles but is also a simple consequence of geometric projection. Figure 20 reveals similar results for other wind models. The curves rise so steeply that the effects of slit-loss are minor (order unity) unless the slit-width is very small. Nevertheless, the results

do motivate extended aperture observations, e.g. integral field unit (IFU) instrumentation, that would map the wind both spatially and spectrally.

Although several effects can reduce the line-emission relative to the absorption of the outflow, our analysis indicates that detectable line-emission should occur frequently. Furthermore, the line-emission could be suppressed so that it does not exceed the galaxy continuum yet still (partially) fills-in the absorption profiles. Indeed, dust and anisotropic winds preferentially suppress line-emission at $\delta v > 0 \text{ km s}^{-1}$ (Figures 8,10). The remaining emission would still modify the observed absorption profiles (e.g. Figure 5) and may complicate conclusions regarding characteristics of the flow. *An analysis of cool gas outflows that entirely ignores line-emission may incorrectly conclude that the source is partially covered, that the gas has a significantly lower peak optical depth, and/or that a $\delta v \sim 0 \text{ km s}^{-1}$ component is absent.* We now examine several quantitative effects of line-emission.

Figure 21 demonstrates one observational consequence: reduced measurements for the absorption equivalent

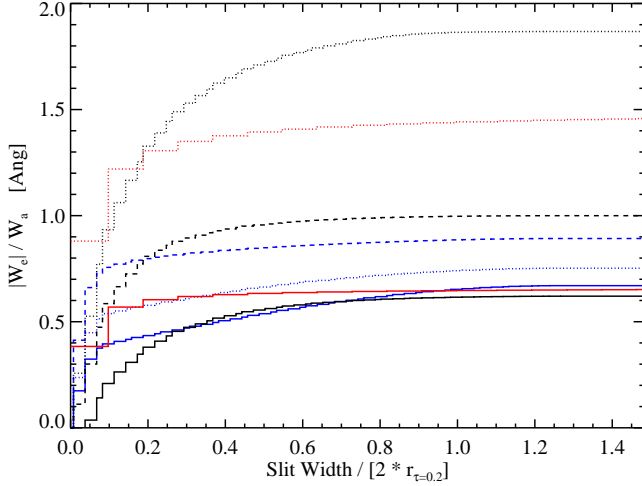


FIG. 20.— Absolute emission equivalent width ($|W_e|$) relative to the observed absorption equivalent width (W_a) for a series of transitions: (solid – Mg II $\lambda 2796$; dotted – Mg II $\lambda 2803$; dashed – Fe II $\lambda 2600$). The W_e/W_a ratio is plotted as a function of slit width relative to twice the radius $r_{\tau_S=0.2}$, defined to be where the Sobolev optical depth $\tau_S = 0.2$. The black curves correspond to the fiducial wind model (§ 3; $r_{\tau_S=0.2} \approx 15$ kpc), the red curves are for the LBG-partial covering scenario (§ 5.1.2; $r_{\tau_S=0.2} \approx 8$ kpc), and the radiation-driven wind (§ 5.2; $r_{\tau_S=0.2} = 40$ kpc) has blue curves. For all of the wind models, the $|W_e|/W_a$ ratio rises very steeply with slit width and then plateaus at $\approx r_{\tau_S=0.2}$. Therefore, a slit that exceeds $\approx 0.5r_{\tau_S=0.2}$ will admit nearly all of the photons scattered to our sightline.

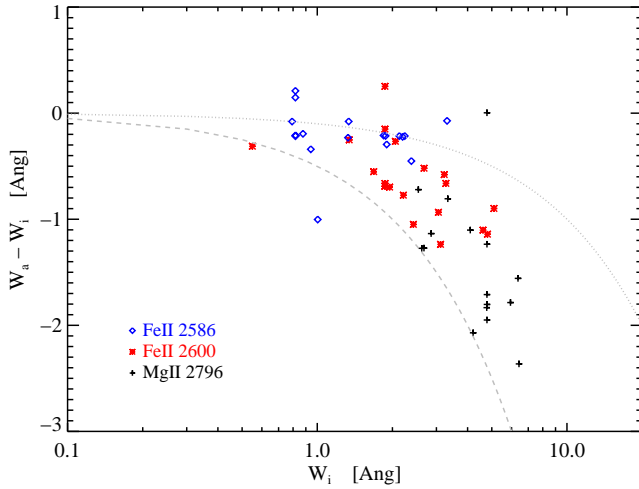


FIG. 21.— Difference between the ‘observed’ absorption equivalent width W_a which includes the flux of scattered photons and the ‘intrinsic’ equivalent width W_i that ignores photon scattering. The dashed (dotted) curves trace a 50% (10%) reduction in W_a relative to W_i . One notes a reduction in W_a by $\approx 30 - 50\%$ for the Mg II $\lambda 2796$ transition (the effect is generally larger for Mg II $\lambda 2803$). The effects of scattered photons are reduced for the Fe II transitions because a fraction (in fact a majority for Fe II $\lambda 2586$) of the absorbed photons fluoresce as Fe II* emission at longer wavelengths and do not ‘fill-in’ the absorption profiles. The figure shows results for all of the models presented in Tables 4 and 6.

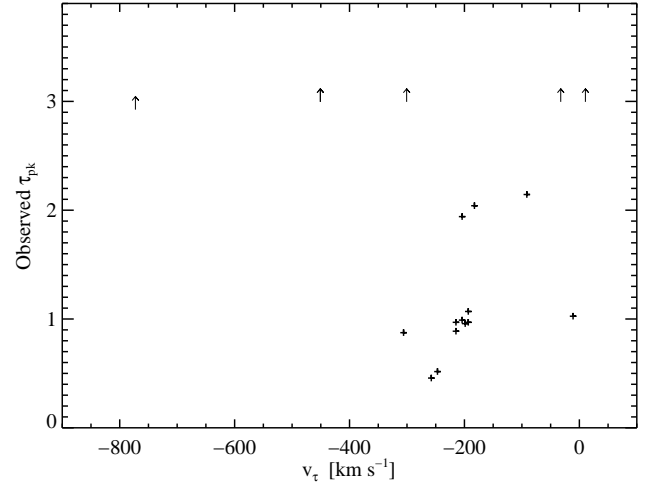


FIG. 22.— The observed peak optical depth $\tau_{pk} \equiv -\ln[I_{\min}]$ for Mg II $\lambda 2796$ profiles of the wind models studied in this paper (Tables 4, 6) with I_{\min} the minimum normalized intensity of the absorption profile. Cases where τ_{pk} exceeds 3 are presented as lower limits. The τ_{pk} values are plotted against the velocity v_τ where $I(v_\tau) = I_{\min}$. In all of the models, the true peak optical depth $\tau_{pk}^{\text{true}} > 10$. The much lower ‘observed’ τ_{pk} values occur because scattered Mg II $\lambda 2796$ photons have filled-in the absorption profiles at velocities $\delta v \gtrsim -400$ km s $^{-1}$. These effects, therefore, are greatest for wind models where the optical depth peaks near $\delta v \sim 0$ km s $^{-1}$ because the majority of scattered photons have this relative velocity. Indeed, models with $v_\tau < -400$ km s $^{-1}$ all show $\tau_{pk} > 3$.

width W_a of the flow. In the case of Mg II, which has the most strongly affected transitions, W_a is reduced by 30–50% from the intrinsic equivalent width (the equivalent width one would measure in the absence of scattered photons). In turn, one may derive a systematically lower optical depth or velocity extent for the wind, and therefore a lower total mass and kinetic energy. The effects are most pronounced for wind scenarios where the peak optical depth occurs near $\delta v = 0$ km s $^{-1}$. Geometric projection limits the majority of scattered photon emission to have $|\delta v| < 200$ km s $^{-1}$; therefore, the absorption profiles are filled-in primarily at these velocities.

Another (related) consequence is the reduction of the peak depth of absorption. In Figure 22, we plot the observed peak optical depth τ_{pk} for Mg II $\lambda 2796$ versus the velocity where the profile has greatest depth for the various wind models (i.e. τ_{pk} vs. v_τ from Tables 4 and 6). In every one of the models, the true peak optical depth $\tau_{pk}^{\text{true}} > 10$. For the majority of cases with $v_\tau > -300$ km s $^{-1}$, one observes $\tau_{pk} < 2$ and would infer the wind is not even optically thick! This occurs because photons scattered by the wind have ‘filled-in’ the absorption at velocity $\delta v \approx 0$ km s $^{-1}$. In contrast, wind models with $v_\tau < -400$ km s $^{-1}$ all yield $\tau_{pk} > 3$. The results are similar for the Mg II $\lambda 2803$ profile. In fact, one generally measures a similar τ_{pk} for each Mg II line and may incorrectly conclude that the source is partially covered. In the case of Fe II, one may even observe a (non-physical) inversion in the apparent optical depths of Fe II $\lambda 2586$ and Fe II $\lambda 2600$ (e.g. Figure 13).

These effects are reduced for the Fe II absorption profiles, especially for Fe II $\lambda 2586$. This is because a significant fraction (even a majority) of the Fe II emission

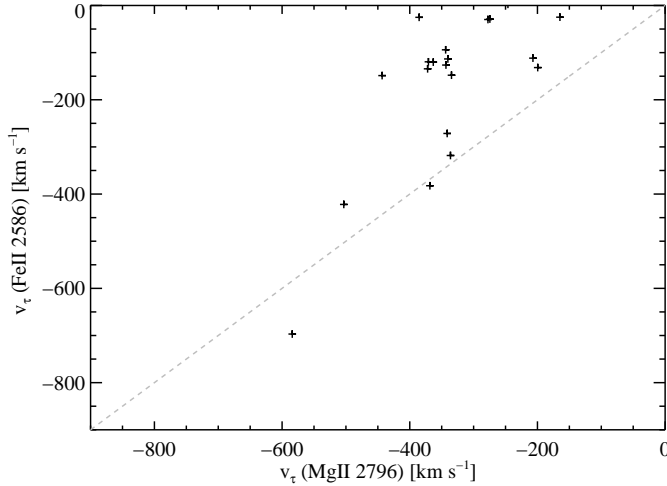


FIG. 23.— Comparison of the velocities for which the Fe II $\lambda 2586$ and Mg II $\lambda 2796$ absorption profiles have greatest depth. Results for all of the models studied in this paper are presented (Tables 4, 6). It is evident that wind models with a peak optical depth near the systemic velocity have a Mg II $\lambda 2796$ absorption profile shifted blueward by one to several hundred km s^{-1} . Analysis of such profiles may lead to the false conclusion that (i) the majority of mass in the wind is travelling at a higher velocity; and (ii) there is no gas with $\delta v \sim 0 \text{ km s}^{-1}$. The dashed curve traces the one-to-one line.

is fluorescent Fe II* emission at longer wavelengths which does not affect the absorption profiles. Therefore, the Fe II absorption equivalent widths (W_a) more closely follow the intrinsic values, one derives more accurate peak optical depths, and the absorption kinematics more faithfully reflect the motions of the flow. Regarding the last point, one also predicts a velocity offset between the Fe II and Mg II absorption-line centroids (Figure 23). This affects the analysis of gas related to the ISM of the galaxy and also material infalling at modest speeds. Figure 23 also emphasizes that the Mg II profiles may misrepresent the kinematics of the bulk of the gas. Analysis of these lines, without consideration of line-emission, may lead to incorrect conclusions on the energetics and mass flux of the wind.

We emphasize that all of these effects are heightened by the relatively low spectral resolution and S/N characteristic of the data commonly acquired for $z > 0$ star-forming galaxies. Figure 24a shows one realization of the Mg II $\lambda\lambda 2796, 2803$ doublet for the ISM+wind model convolved with the line-spread-function of the Keck/LRIS spectrometer (a Gaussian with $\text{FWHM}=250 \text{ km s}^{-1}$) and an assumed signal-to-noise of $S/N=7$ per 1 \AA pixel. Both the absorption and emission are well detected, but it would be difficult to resolve the issues discussed above (e.g. partial covering, peak optical depth) with these data. One also notes several systematic effects of the lower spectral resolution, e.g. reduced peak flux in the line-emission and a systematic shift of Mg II $\lambda 2796$ absorption to more negative velocity. We have also modelled an observation of the ISM+wind model using a stacked galaxy spectrum (Figure 24b). Specifically, we averaged 100 identical Mg II profiles from the fiducial model degraded to a $S/N=2 \text{ pix}^{-1}$ and shifted by a random velocity offset with $\sigma = 100 \text{ km s}^{-1}$. This treatment illustrates the ef-

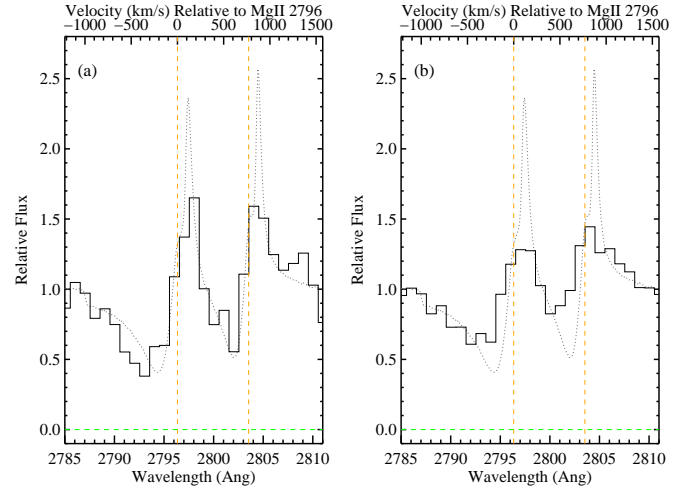


FIG. 24.— ‘Observations’ of the Mg II profiles for the ISM+wind model. (a) The true profile (dotted lines) has been convolved with a Gaussian line-spread-function ($\text{FWHM} = 250 \text{ km s}^{-1}$) and noise has been added to give a $S/N=7$ per pixel. Note the suppressed peak in line-emission; one may even infer the flux of Mg II $\lambda 2796$ exceeds that of Mg II $\lambda 2803$. The Mg II $\lambda 2796$ absorption is also shifted to shorter wavelengths, i.e. to a greater velocity offset from systemic. (b) The solid curve shows a stack of 100 spectra of the ISM+wind profile, each degraded to a $S/N=2$ per pixel, and offset from systemic by a normal deviate with $\sigma = 100 \text{ km s}^{-1}$ to mimic uncertainty in the redshift of the galaxies. This treatment is meant to illustrate the implications of stacking galaxy spectra to study outflows (e.g. Weiner et al. 2009; Rubin et al. 2010b, S10). The main difference from the single galaxy observation shown in panel (a) is the smearing of line-emission and absorption that reduces the height/depth of each. The effects would likely be even more pronounced if one studied spectra with a diversity of Mg II profiles.

fects of using stacked galaxy spectra to study outflows (e.g. Weiner et al. 2009; Rubin et al. 2010b, S10). The main difference between this and the single galaxy observation shown in panel (a) is the smearing of line-emission and absorption that reduces the height/depth of each. The effects would be even more pronounced if one studied spectra with a diversity of Mg II profiles. Special care is required, therefore, to interpret properties of the wind (and ISM) from such spectral analysis.

The previous few paragraphs sounded a cautionary perspective on the implications for absorption-line analysis of galactic-scale outflows in the presence of (expected) significant line-emission. While this is a necessary complication, we emphasize that such analysis remains one of the few observational techniques at our disposal to study outflows. Furthermore, direct analysis of the line-emission offers new and unique constraints on the characteristics of the outflow. And, when coupled with the absorption-line data, the two sets of constraints may break various degeneracies in the physical characteristics of the outflow. We now consider a few examples.

The most obvious characteristics probed by the line-emission are the size and morphology of the outflow (Rubin et al. 2010a). Line emission is predicted to extend to radii where the Sobolev optical depth exceeds a few tenths. The principle challenge is to achieve sufficient sensitivity to detect the predicted, low surface-brightness emission. As Figure 25 demonstrates, the surface brightness at the inner wind radius of our fiducial wind exceeds that at the outer radius by several orders of magnitude. Nevertheless, an instrument that sampled the entire wind

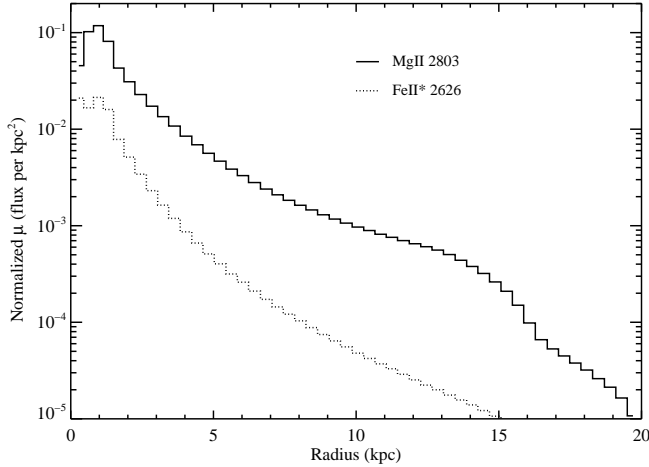


FIG. 25.— Surface brightness profiles of the fiducial wind model for the Mg II $\lambda 2796$ (solid) and Fe II* $\lambda 2626$ (dotted) transitions. Both profiles peak at small radii and decrease by several orders of magnitude before reaching the outer edge of the wind. The profiles are sufficiently shallow, however, that the azimuthally integrated flux declines by only a factor of ≈ 10 from $r = 1$ kpc to $r = 10$ kpc. Therefore, a sensitive IFU observation could map the emission (and, in principle, the kinematics) from r_{inner} to approximately r_{outer} .

(e.g. a large format IFU or narrow band imager) may detect the emission in azimuthally-averaged apertures. For the fiducial wind model, for example, the azimuthally integrated flux falls by only a factor of 10 for projected radii of 1 to 15 kpc. Of the transitions considered in this paper, Mg II emission is preferred for this analysis because (i) it has the largest equivalent width in absorption and (ii) there are fewer emission channels per absorption line than for Fe II. The Mg II lines (especially Mg II $\lambda 2803$) frequently have the highest peak and integrated fluxes (Figure 25). On the other hand, the Mg II transitions are more susceptible to the effects of dust extinction and for some galaxies Fe II* emission could be dominant. In either case, the study of spatially-extended line-emission from photons scattered by a galactic-scale wind offers a direct means to study the morphology and radial extent of these phenomena. The next generation of large-format optical and infrared integral-field-units are well-suited to this scientific endeavor (e.g. KCWI on Keck, MUSE on the VLT).

The kinematic measurements of the line-emission also offer insight into physical characteristics of the wind. In § 4.2, we emphasized that dust extinction preferentially suppresses photons scattered off the backside of the wind (e.g. $\delta v > 0$ km s $^{-1}$) so that the line-centroid is shifted to negative velocities. Similarly, anisotropic models with reduced emission off the backside yield emission lines that are centered blueward of the galaxy’s systemic redshift. These effects are most prominent in the Fe II* emission. The centroids of the Mg II lines, meanwhile, are sensitive to the optical depth profile of the wind. For example, a wind with flows exceeding ≈ 600 km s $^{-1}$ will shift the Mg II $\lambda 2796$ centroid to bluer wavelengths (e.g. Figure 13). Although these effects are modest (tens of km s $^{-1}$), they may be resolved by moderate resolution spectroscopy.

The emission-line velocity widths also reveal charac-

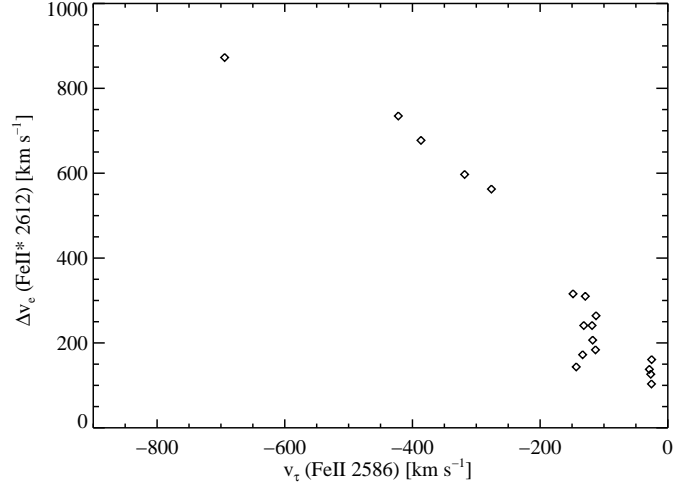


FIG. 26.— Plot of the 90% velocity width (Δv_e) of Fe II* $\lambda 2612$ emission versus the velocity where the resonance lines achieve peak optical depth v_τ in absorption. The Δv_e values rise steadily with increasing offset of v_τ from systemic. The width of the Fe II* $\lambda 2612$ emission line, therefore, offers an independent diagnostic of the wind speed.

teristics of the wind. In particular, the Fe II* emission-line widths are sensitive to the optical depth of the wind at large velocity offsets from systemic. This is illustrated in Figure 26 which plots the 90% velocity width Δv_e of Fe II* $\lambda 2612$ versus the velocity where the wind optical depth is maximal (v_τ). We find that Δv_e increases with v_τ such that a large width for Fe II* emission requires a wind profile with large optical depths at $\delta v < -200$ km s $^{-1}$. The broadening of Fe II* emission occurs because this emission is dominated by single scatterings which trace all components of the wind.

Lastly, the line flux ratios of pairs of transitions are sensitive to characteristics of the wind. The most obvious example is the relative emission of the Mg II $\lambda\lambda 2796, 2803$ doublet. Specifically, an outflow whose velocity exceeds the doublet spacing ($\Delta v \approx 770$ km s $^{-1}$) will convert Mg II $\lambda 2796$ photons into Mg II $\lambda 2803$ emission resulting in a flux ratio that is inverted relative to the intrinsic optical depth profiles (e.g. Figure 13). Another important example is the relative flux of Fe II* emission relative to Mg II. A dusty medium with velocity near systemic (e.g. an ISM component) may significantly suppress Mg II emission yet have a significant Fe II* line flux because the latter is not resonantly trapped.

7. SUMMARY

In this paper, we have explored the predicted absorption and emission-line profiles of a set of simple galactic-scale outflow models. This analysis implemented Monte Carlo radiative transfer techniques to propagate resonant photons through an expanding medium, allowing for their conversion to non-resonant photons (e.g. Fe II*). Our work focused on the Mg II $\lambda\lambda 2796, 2803$ and Fe II UV1 multiplet of rest-frame UV transitions, but the results apply to most other lines used to probe cool gas. Our primary findings are summarized as follows:

1. Isotropic, dust-free wind models conserve photon flux. Therefore, the blue-shifted absorption-line profiles commonly observed in star-forming galax-

- ies are predicted to be accompanied by emission-lines with similar equivalent width. This holds even for non-extreme anisotropic and dust-extincted scenarios.
2. The line-emission occurs preferentially at the systemic velocity of the galaxy and ‘fills-in’ the absorption profiles at velocity offsets $|\delta v| < 200 \text{ km s}^{-1}$ from systemic. For transitions that are only coupled to the ground-state (e.g. Mg II, Ly α , Na I), this implies much lower, absorption-line equivalent widths (by up to 50%) and observed absorption profiles that are significantly offset in velocity from the intrinsic optical depth profile.
 3. Analysis of cool gas outflows that entirely ignores this line-emission may incorrectly conclude that the source is partially covered, that the gas has a significantly lower peak optical depth, and/or that gas with velocities near systemic (e.g. from the ISM or even an infalling component) is absent.
 4. Resonance transitions that are strongly coupled to non-resonant lines (e.g. Fe II, Si II) produce emission dominated by the optically-thin, fine-structure transitions. As such, these resonance absorption lines offer the best characterization of the opacity of the wind and also of gas with velocities near systemic.
 5. Dust extinction modestly affects models where resonance photons are trapped for only a few scatterings. Models with high opacity at small radii and at systemic velocity (e.g. with an optically thick, ISM component) can effectively extinguish resonantly trapped emission (Mg II) but have weaker effect on non-resonant lines (Fe II*).
 6. We examined two scenarios designed to mimic the wind model proposed by Steidel et al. (2010) for $z \sim 3$ Lyman break galaxies. Our implementation of this model generates substantial line-emission from scattered photons that greatly modifies the predicted line-profiles so that this model does not reproduce the observed line-profiles.
 7. Significant line-emission is a generic prediction of simple wind models, even in the presence of dust, anisotropic flows, and when viewed through finite apertures. We have explored the 2D emission maps (Figure 6) and surface brightness profiles (Figure 25) of the winds. Sensitive, spatially-extended observations will map the morphology and radial extent of the outflows. These data afford the best opportunity to estimate the energetics and mass-flux of galactic-scale outflows.
 8. The kinematics and flux ratios of the emission lines constrain the speed, opacity, dust extinction, and morphology of the wind. When combined with absorption-line analysis, one may develop yet tighter constraints on these characteristics.

We acknowledge valuable conversations with D. Koo, J. Hennawi, A. Coil, and A. Wolfe. J.X.P and K.R. are partially supported by an NSF CAREER grant (AST-0548180), and by NSF grant AST-0908910.

REFERENCES

- Aguirre, A., Hernquist, L., Schaye, J., Weinberg, D. H., Katz, N., & Gardner, J. 2001, *ApJ*, 560, 599
- Alton, P. B., Davies, J. I., & Bianchi, S. 1999, *A&A*, 343, 51
- Charlot, S., & Fall, S. M. 2000, *ApJ*, 539, 718
- Chen, Y., Tremonti, C. A., Heckman, T. M., Kauffmann, G., Weiner, B. J., Brinchmann, J., & Wang, J. 2010, *AJ*, 140, 445
- Chevalier, R. A., & Clegg, A. W. 1985, *Nature*, 317, 44
- Dijkstra, M., Haiman, Z., & Spaans, M. 2006, *ApJ*, 649, 14
- France, K., Nell, N., Green, J. C., & Leitherer, C. 2010, *ApJ*, 722, L80
- Fujita, A., Martin, C. L., Mac Low, M., New, K. C. B., & Weaver, R. 2009, *ApJ*, 698, 693
- Hamann, F., Kanekar, N., Prochaska, J. X., Murphy, M. T., Ellison, S., Malec, A. L., Milutinovic, N., & Ubachs, W. 2010, *ArXiv e-prints*
- Harrington, J. P. 1973, *MNRAS*, 162, 43
- Hartigan, P., Morse, J. A., Tumlinson, J., Raymond, J., & Heathcote, S. 1999, *ApJ*, 512, 901
- Heckman, T. M., Armus, L., & Miley, G. K. 1990, *ApJS*, 74, 833
- Hughes, D. H., Robson, E. I., & Gear, W. K. 1990, *MNRAS*, 244, 759
- Jeffery, D. J., & Branch, D. 1990, in *Supernovae*, Jerusalem Winter School for Theoretical Physics, ed. J. C. Wheeler, T. Piran, & S. Weinberg, 149–
- Kasen, D., Branch, D., Baron, E., & Jeffery, D. 2002, *ApJ*, 565, 380
- Kasen, D., Thomas, R. C., & Nugent, P. 2006, *ApJ*, 651, 366
- Kasen, D., & Woosley, S. E. 2007, *ApJ*, 656, 661
- . 2009, *ApJ*, 703, 2205
- Kasen, D., et al. 2010, *ApJ* in preparation
- Kereš, D., Katz, N., Davé, R., Fardal, M., & Weinberg, D. H. 2009, *MNRAS*, 396, 2332
- Kinney, A. L., Bohlin, R. C., Calzetti, D., Panagia, N., & Wyse, R. F. G. 1993, *ApJS*, 86, 5
- Kobulnicky, H. A., & Martin, C. L. 2010, *ApJ*, 718, 724
- Kurucz, R. L. 2005, *Memorie della Societa Astronomica Italiana Supplementi*, 8, 14
- Laursen, P., Razoumov, A. O., & Sommer-Larsen, J. 2009, *ApJ*, 696, 853
- Lehnert, M. D., Heckman, T. M., & Weaver, K. A. 1999, *ApJ*, 523, 575
- Lowenthal, J. D., et al. 1997, *ApJ*, 481, 673
- Martin, C. L. 1999, *ApJ*, 513, 156
- . 2005, *ApJ*, 621, 227
- Martin, C. L., & Bouché, N. 2009, *ApJ*, 703, 1394
- Ménard, B., Nestor, D., Turnshek, D., Quider, A., Richards, G., Chelouche, D., & Rao, S. 2008, *MNRAS*, 385, 1053
- Ménard, B., Scranton, R., Fukugita, M., & Richards, G. 2010, *MNRAS*, 405, 1025
- Morton, D. C. 2003, *ApJS*, 149, 205
- Murray, N., Ménard, B., & Thompson, T. A. 2010, *ArXiv e-prints*
- Murray, N., Quataert, E., & Thompson, T. A. 2005, *ApJ*, 618, 569
- Neufeld, D. A. 1990, *ApJ*, 350, 216
- Nulsen, P. E. J., Barcons, X., & Fabian, A. C. 1998, *MNRAS*, 301, 168
- Oppenheimer, B. D., & Davé, R. 2006, *MNRAS*, 373, 1265
- Pettini, M., Kellogg, M., Steidel, C. C., Dickinson, M., Adelberger, K. L., & Giavalisco, M. 1998, *ApJ*, 508, 539
- Pettini, M., Rix, S. A., Steidel, C. C., Adelberger, K. L., Hunt, M. P., & Shapley, A. E. 2002, *ApJ*, 569, 742
- Pettini, M., Steidel, C. C., Adelberger, K. L., Dickinson, M., & Giavalisco, M. 2000, *ApJ*, 528, 96
- Phillips, A. C. 1993, *AJ*, 105, 486
- Prochaska, J. X., Chen, H.-W., & Bloom, J. S. 2006, *ApJ*, 648, 95

- Prochaska, J. X., Chen, H.-W., Dessauges-Zavadsky, M., & Bloom, J. S. 2007, *ApJ*, 666, 267
- Prochaska, J. X., & Wolfe, A. M. 2001, *ApJ*, 560, L33
- Radovich, M., Kahanpää, J., & Lemke, D. 2001, *A&A*, 377, 73
- Rubin, K. H. R., Prochaska, J. X., Ménard, B., Murray, N., Kasen, D., Koo, D. C., & Phillips, A. C. 2010a, *ArXiv e-prints*
- Rubin, K. H. R., Weiner, B. J., Koo, D. C., Martin, C. L., Prochaska, J. X., Coil, A. L., & Newman, J. A. 2010b, *ApJ*, 719, 1503
- Rupke, D. S., Veilleux, S., & Sanders, D. B. 2005a, *ApJS*, 160, 87
- . 2005b, *ApJS*, 160, 115
- Sato, T., Martin, C. L., Noeske, K. G., Koo, D. C., & Lotz, J. M. 2009, *ApJ*, 696, 214
- Savage, B. D., & Sembach, K. R. 1996, *ARA&A*, 34, 279
- Scannapieco, E., Pichon, C., Aracil, B., Petitjean, P., Thacker, R. J., Pogosyan, D., Bergeron, J., & Couchman, H. M. P. 2006, *MNRAS*, 365, 615
- Schaye, J. 2001, *ApJ*, 559, L1
- Shapley, A. E., Steidel, C. C., Pettini, M., & Adelberger, K. L. 2003, *ApJ*, 588, 65
- Silva, A. I., & Viegas, S. M. 2002, *MNRAS*, 329, 135
- Simcoe, R. A., Sargent, W. L. W., & Rauch, M. 2002, *ApJ*, 578, 737
- Snow, T. P., Lamers, H. J. G. L. M., Lindholm, D. M., & Odell, A. P. 1994, *ApJS*, 95, 163
- Sobolev, V. V. 1960, *Moving envelopes of stars*
- Socrates, A., Davis, S. W., & Ramirez-Ruiz, E. 2008, *ApJ*, 687, 202
- Somerville, R. S., Primack, J. R., & Faber, S. M. 2001, *MNRAS*, 320, 504
- Steidel, C. C., Erb, D. K., Shapley, A. E., Pettini, M., Reddy, N., Bogosavljević, M., Rudie, G. C., & Rakic, O. 2010, *ApJ*, 717, 289
- Steidel, C. C., Giavalisco, M., Pettini, M., Dickinson, M., & Adelberger, K. L. 1996, *ApJ*, 462, L17+
- Strickland, D. K., & Heckman, T. M. 2009, *ApJ*, 697, 2030
- Strickland, D. K., Heckman, T. M., Colbert, E. J. M., Hoopes, C. G., & Weaver, K. A. 2004, *ApJ*, 606, 829
- Swinbank, A. M., et al. 2005, *MNRAS*, 359, 401
- Tasitsiomi, A. 2006, *ApJ*, 645, 792
- Tremonti, C. A., Moustakas, J., & Diamond-Stanic, A. M. 2007, *ApJ*, 663, L77
- Veilleux, S., Shopbell, P. L., Rupke, D. S., Bland-Hawthorn, J., & Cecil, G. 2003, *AJ*, 126, 2185
- Verhamme, A., Schaerer, D., & Maselli, A. 2006, *A&A*, 460, 397
- Walter, F., Weiss, A., & Scoville, N. 2002, *ApJ*, 580, L21
- Weiner, B. J., et al. 2009, *ApJ*, 692, 187
- Westmoquette, M. S., Smith, L. J., & Gallagher, J. S. 2008, *MNRAS*, 383, 864
- York, D. G., et al. 2006, *MNRAS*, 367, 945
- Zheng, Z., & Miralda-Escudé, J. 2002, *ApJ*, 578, 33